Supplementary Materials for

Quantum spectroscopy of topological dynamics via a supersymmetric Hamiltonian

Hiroshi Yamauchi[1,5*], Satoshi Kanno[1], Yuki Sato[2], Hiroyuki Tezuka[3,5], Yoshi-aki Shimada[1], Eriko Kaminishi[5], Naoki Yamamoto[4,5]

[1]SoftBank Corp., Research Institute of Advanced Technology, 1-7-1 Kaigan, Minato-ku, Tokyo 105-7529, Japan

[2]Toyota Central R&D Labs., Inc., 1-4-14, Koraku, Bunkyo-ku, Tokyo, 112-0004, Japan

[3]Advanced Research Laboratory, Sony Group Corporation, 1-7-1 Konan, Minato-ku, Tokyo 108-0075, Japan

[4]Department of Applied Physics and Physico-Informatics, Keio University, 3-14-1 Hiyoshi, Kohoku-ku, Yokohama, Kanagawa 223-8522, Japan

[5]Quantum Computing Center, Keio University, 3-14-1 Hiyoshi, Kohoku-ku, Yokohama, Kanagawa 223-8522, Japan

[*]Corresponding author: hiroshi.yamauchi@g.softbank.co.jp

This PDF file includes the following:

Materials and methods

Contents (Main Text + Supplement)

Main Text

S1 Hodge Laplacian and Homology

Let K be a finite, oriented simplicial complex. For each $k \geq 0$, the k–chain space $C_k(K)$ is the real vector space spanned by oriented k–simplices, equipped with the inner product that makes those simplices orthonormal. The boundary operators

$$\partial_k : C_k \to C_{k-1}, \qquad \partial_k [v_0, \ldots, v_k] = \sum_{i=0}^{k} (-1)^i [v_0, \ldots, \widehat{v_i}, \ldots, v_k] \tag{S1}$$

assemble into the chain complex

$$\cdots \xrightarrow{\partial_{k+1}} C_k \xrightarrow{\partial_k} C_{k-1} \xrightarrow{\partial_{k-1}} \cdots, \qquad \partial_k \partial_{k+1} = 0. \tag{S2}$$

The kth homology group is

$$H_k(K) = \ker(\partial_k)/\mathrm{im}(\partial_{k+1}), \qquad \beta_k = \dim H_k(K), \tag{S3}$$

which counts independent k–dimensional holes (*54*). In Eq. (S1), $\widehat{v_i}$ indicates omission of v_i, and the orientation is the canonical orientation induced by the vertex order.

With respect to the chosen inner product, let $\partial_k^\dagger$ denote the adjoint of ∂_k. It is convenient to split the k–Hodge Laplacian into its "down" and "up" parts and write

$$L_k^\downarrow = \partial_k^\dagger \partial_k, \qquad L_k^\uparrow = \partial_{k+1} \partial_{k+1}^\dagger, \qquad L_k = L_k^\downarrow + L_k^\uparrow = \partial_k^\dagger \partial_k + \partial_{k+1} \partial_{k+1}^\dagger, \tag{S4}$$

All operators act on $C_k(K)$ equipped with the simplex-orthonormal inner product, so $(\cdot)^\dagger$ is just transposed with respect to that basis.

Any k–chain $x \in C_k$ admits three qualitatively distinct behaviors. It can be a *gradient* (an exact k–chain) of some $(k-1)$–chain, $x = \partial_k^\dagger y$; it can be a *curl* (a coexact k–chain) induced by a $(k+1)$–chain, $x = \partial_{k+1} z$; or it can simultaneously cycle and cocycle, i.e., $x \in \ker(\partial_k) \cap \ker(\partial_{k+1}^\dagger)$, which is divergence–free and curl–free. The latter are the *harmonic* k–chains and encode the homology.

The Hodge decomposition states that these three subspaces are mutually orthogonal and span C_k:

$$C_k \;=\; \mathrm{im}(\partial_k^\dagger) \,\oplus\, \ker L_k \,\oplus\, \mathrm{im}(\partial_{k+1}), \qquad \ker L_k = \ker(\partial_k) \cap \ker(\partial_{k+1}^\dagger) \cong H_k, \quad \beta_k = \dim \ker L_k. \tag{S5}$$

Thus every $x \in C_k$ splits uniquely as $x = x_{\mathrm{grad}} + x_{\mathrm{harm}} + x_{\mathrm{curl}}$, with the three components pairwise orthogonal.

Because the direct sum is orthogonal, each component can be recovered via orthogonal projection. Using Moore–Penrose pseudoinverses,

$$P_{\mathrm{grad}} = \partial_k^\dagger (\partial_k \partial_k^\dagger)^+ \partial_k, \qquad P_{\mathrm{curl}} = \partial_{k+1} (\partial_{k+1}^\dagger \partial_{k+1})^+ \partial_{k+1}^\dagger, \tag{S6}$$

$$P_{\mathrm{harm}} = I - P_{\mathrm{grad}} - P_{\mathrm{curl}}, \qquad x_\bullet = P_\bullet x. \tag{S7}$$

Equivalently, $x_{\mathrm{grad}} = \partial_k^\dagger u$ where u solves the normal equations $\partial_k \partial_k^\dagger u = \partial_k x$; $x_{\mathrm{curl}} = \partial_{k+1} v$ where $\partial_{k+1}^\dagger \partial_{k+1} v = \partial_{k+1}^\dagger x$; and x_{harm} is the residual in $\ker L_k$.

The appearance of the adjoint $\partial_k^\dagger$ in P_{grad} is deliberate and fundamental. Since $\mathrm{im}(\partial_k^\dagger)$ is the subspace of exact k–cochains (coboundaries), projection onto this space necessarily involves $\partial_k^\dagger$ acting on the left. Had we used ∂_k instead, the resulting operator would project onto $\mathrm{im}(\partial_k)$, the boundary subspace associated with the next lower chain group, corresponding to P_{curl}. Thus the two projectors are adjoint counterparts under discrete Hodge pairing:

$$P_{\mathrm{grad}} = \partial_k^\dagger (\partial_k \partial_k^\dagger)^+ \partial_k, \qquad P_{\mathrm{curl}} = \partial_{k+1} (\partial_{k+1}^\dagger \partial_{k+1})^+ \partial_{k+1}^\dagger.$$

This construction ensures that P_{grad}, P_{curl}, and P_{harm} form a complete, mutually orthogonal decomposition of C_k, as guaranteed by the Hodge theorem for finite complexes. Equivalent formulations appear in the discrete Hodge-theoretic treatments of Horak and Jost (*55*) and Lim (*56*), where the operators are written as

$$P_{\mathrm{grad}} = \delta (\delta^* \delta)^+ \delta^*, \qquad P_{\mathrm{curl}} = \delta^* (\delta \delta^*)^+ \delta,$$

where $\delta = \partial_k^\dagger$ denotes the coboundary operator.

For the case where $k = 1$, write B_1 for the vertex–edge incidence matrix and B_2 for the edge–triangle incidence matrix of K (if triangles are present). Let $B_1 \in \mathbb{R}^{|V|\times|E|}$ be the vertex–edge incidence (each column has one +1 and one −1 according to edge orientation), and $B_2 \in \mathbb{R}^{|E|\times|T|}$ the edge–triangle incidence (entries in $\{0, \pm 1\}$ given by compatible orientation). Then

$$L_1^{\downarrow} = B_1^{\top} B_1, \qquad L_1^{\uparrow} = B_2 B_2^{\top}, \qquad L_1 = B_1^{\top} B_1 + B_2 B_2^{\top}. \tag{S8}$$

Here $\mathrm{im}(B_1^{\top})$ consists of edge differences of a scalar potential on vertices (gradient space), $\mathrm{im}(B_2)$ consists of circulations induced by triangle potentials (curl space), and $\ker L_1$ consists of edge flows that are both divergence–free ($B_1 x = 0$) and curl–free ($B_2^{\top} x = 0$); hence $\beta_1 = \dim \ker L_1$ recovers the first Betti number. On a pure graph with no filled triangles ($B_2 = 0$), one simply has $L_1 = B_1^{\top} B_1$ and $\ker L_1 = \ker B_1$, the usual cycle space (*57, 58*).

The Hodge Laplacian introduced above not only decomposes chains into gradient, curl, and harmonic components but also connects directly to the semiclassical picture of Witten–Morse supersymmetric quantum mechanics (*29*). In this correspondence, the gradient, curl, and harmonic parts represent, respectively, downwards and upwards gradient flows and the stationary (zero–energy) sector of a supersymmetric Hamiltonian. Under Witten's deformation $d_t = e^{-tf} d e^{tf}$ the Laplacian $\Delta_t = (d_t + d_t^{\dagger})^2$ acquires exponentially small eigenvalues $E_i(t) \sim \exp[-2t\,\Delta f_i/\hbar]$ generated by tunneling between distinct basins of the Morse function f. The first nonzero eigenvalue therefore measures a tunneling gap that quantifies how strongly separated topological sectors communicate. In the discrete combinatorial setting this role is played by

$$\Delta_{\mathrm{SUSY}}^{(1)} = \min\{\lambda > 0 : \lambda \in \sigma(L_1)\},$$

the smallest positive eigenvalue of the one–form Hodge block. When persistent loops are well isolated in geometry, tunneling is suppressed and the gap widens; when loops merge or collapse, tunneling increases and the gap closes. Across a filtration or control parameter this gap $\Delta_{\mathrm{SUSY}}^{(1)}$ typically covaries with the highest persistence of homology $\ell_{H_1}^{\max}$, providing a spectral proxy for topological stability (*32, 59*). This connection unifies the classical Hodge decomposition, the Witten–Morse

semiclassical analysis, and modern persistent-Laplacian formulations into a single framework linking gradient flow, tunneling amplitude, and topological persistence.

From a spectral viewpoint, eigenpairs of L_k separate according to (S5): harmonic modes ($\lambda = 0$) span homology, whereas nonzero eigenvalues arise from gradient–type subspaces and curl–type subspaces (*32,54,55,60*). Small but nonzero eigenvalues can come from either block or reflect different geometric mechanisms (e.g., thin bridges versus wide vortical regions). Consequently, interpreting "small eigenvalues" requires tracking their provenance across scales or filtrations; disentangling the three families is essential for faithful geometric and topological inference (*18, 32, 44, 61–65*). Relatedly, persistent homology allows quantitative connections to fractal dimensions via upper box dimension estimates (*66*).

S2 Supersymmetric (SUSY) Hamiltonian and Homology

We consider $\mathcal{N}$=2 supersymmetric quantum mechanics on a $\mathbb{Z}$–graded Hilbert space; F is the degree operator so that $[F, Q] = Q$ shifts degree by +1 and $[F, Q^\dagger] = -Q^\dagger$ by −1.

$$\mathcal{H} = \bigoplus_{k=0}^{m} \mathcal{H}_k, \tag{S9}$$

with odd supercharges Q and $Q^\dagger$ obeying

$$Q^2 = (Q^\dagger)^2 = 0, \qquad H = \{Q, Q^\dagger\} = Q^\dagger Q + Q Q^\dagger, \qquad [F, Q] = Q,\ [F, Q^\dagger] = -Q^\dagger, \tag{S10}$$

where F is the degree operator. Hence $Q : \mathcal{H}_k \to \mathcal{H}_{k+1}$ and $Q^\dagger : \mathcal{H}_k \to \mathcal{H}_{k-1}$, and $[H, F] = 0$ so H is block-diagonal in degree.

Let $d_k := Q\big|_{\mathcal{H}_k} : \mathcal{H}_k \to \mathcal{H}_{k+1}$ and $d_k^\dagger := Q^\dagger\big|_{\mathcal{H}_{k+1}} : \mathcal{H}_{k+1} \to \mathcal{H}_k$, and let P_k be the projector onto $\mathcal{H}_k$. Expanding $Q = \sum_j d_j P_j$ and $Q^\dagger = \sum_j d_{j-1}^\dagger P_j$, for any $v \in \mathcal{H}_k$ we have

$$Hv = (Q^\dagger Q + Q Q^\dagger)v = Q^\dagger(d_k v) + Q(d_{k-1}^\dagger v) = d_k^\dagger d_k v + d_{k-1} d_{k-1}^\dagger v \in \mathcal{H}_k. \tag{S11}$$

Thus, in the degree-k subspace, the SUSY Hamiltonian block equals the k–Hodge Laplacian $\mathcal{L}_k$ acting on k–cochains.

$$H\big|_{\mathcal{H}_k} = d_k^\dagger d_k + d_{k-1} d_{k-1}^\dagger \ = \ \mathcal{L}_k. \tag{S12}$$

At the ends of the complex, $d_{-1} \equiv 0$ and $d_m \equiv 0$, giving $H\big|_{\mathcal{H}_0} = d_0^\dagger d_0$ and $H\big|_{\mathcal{H}_m} = d_{m-1} d_{m-1}^\dagger$.

Positivity follows immediately: for $v \in \mathcal{H}_k$,

$$\langle v, Hv \rangle = \|d_k v\|^2 + \|d_{k-1}^\dagger v\|^2 \geq 0, \tag{S13}$$

Here, $\langle \cdot, \cdot \rangle$ is the Hilbert–space inner product; positivity holds since each term is a squared norm, so $E = 0$ if $d_k v = 0$ and $d_{k-1}^\dagger v = 0$, i.e.,

$$\ker H\big|_{\mathcal{H}_k} = \ker d_k \cap \ker d_{k-1}^\dagger = \ker \mathcal{L}_k. \tag{S14}$$

Zero-energy states are therefore simultaneously closed and coclosed (harmonic).

We use $d_k := Q|_{\mathcal{H}_k}$ and $d_k^\dagger := Q^\dagger|_{\mathcal{H}_{k+1}}$, which is consistent with the coboundary on cochains. Introduce the Q–cohomology

$$H^k(Q) = \ker d_k / \operatorname{im} d_{k-1}. \tag{S15}$$

The Hodge decomposition yields, for every $v \in \mathcal{H}_k$,

$$v = d_{k-1} u + h + d_k^\dagger w, \qquad u \in \mathcal{H}_{k-1},\ w \in \mathcal{H}_{k+1},\ h \in \ker \mathcal{L}_k. \tag{S16}$$

If v is d_k–closed, then v is cohomologous to the unique harmonic representative h; hence, the map $[v] \mapsto h$ induces an isomorphism

$$\ker H\big|_{\mathcal{H}_k} = \ker \mathcal{L}_k \cong H^k(Q) \quad \text{(and by duality } H_k\text{)}, \qquad \dim \ker H\big|_{\mathcal{H}_k} = \beta_k. \tag{S17}$$

All positive–energy levels appear in adjacent–degree pairs: if $Hv = Ev$ with $E > 0$, then Qv and $Q^\dagger v$ (when nonzero) are eigenvectors with the same E in degrees $k{+}1$ and $k{-}1$, respectively; only the harmonic sector contributes to $E = 0$.

When the graded Hilbert space is realized as cochains on a finite simplicial complex and d_k is the coboundary, the block identity (S12) coincides with the combinatorial Hodge Laplacian $\mathcal{L}_k = d_k^\dagger d_k + d_{k-1} d_{k-1}^\dagger$. In particular, for a 1–dimensional block with vertex–edge incidence B_1 and edge–triangle incidence B_2, one has $\mathcal{L}_1 = B_1^\top B_1 + B_2 B_2^\top$; its kernel encodes divergence–free and curl–free edge flows, so $\dim \ker \mathcal{L}_1 = \beta_1$ recovers the cycle space of the underlying complex (and of a pure graph when $B_2 = 0$).

These relations imply a practical dictionary for topology–aware spectroscopy. The degeneracy of zero modes in degree k equals the kth Betti number, whereas the first positive eigenvalue

$$\Delta^{(1)}_{\mathrm{SUSY}} = \min\{\lambda > 0 \mid \lambda \in \sigma(\mathcal{L}_1)\}. \tag{S18}$$

measures the spectral isolation of the corresponding topological sector (an "nearly harmonic" scale). Tracking $\Delta^{(k)}$ and the occupation of $\ker \mathcal{L}_k$ as external parameters (e.g., the Lorenz control ρ) vary suggesting the appearance, merger, or disappearance of topological features in a way that is algebraically exact yet numerically robust.

S3 Dynamical and topological phase transitions of the Lorenz system

We study the Lorenz flow

$$\dot{x} = \sigma(y - x), \qquad \dot{y} = x(\rho - z) - y, \qquad \dot{z} = xy - \beta z. \tag{S19}$$

Here $(\sigma, \beta, \rho) > 0$ are the Prandtl number, the geometric parameter, and the Rayleigh parameter, respectively; we later scan ρ while fixing $(\sigma, \beta) = (10, 8/3)$. For each ρ, a long trajectory yields a point cloud $X(\rho) \subset \mathbb{R}^d$ (either directly in phase space or via delay embedding), and we attach to it a parameter–dependent effective Hamiltonian $H(\rho)$ that captures spectral/dynamical content. This construction allows us to examine phase behavior through two complementary lenses. The *dynamical* lens quantifies how the system explores frequency and state space; the *topological* lens quantifies how the invariant geometry reorganizes across scales. In our experiments we evaluate both families of indicators along ρ and interpret their concordance as evidence for dynamical and topological phase transitions, placing special emphasis on the physical meaning of each indicator.

On the dynamical side, we probe frequency–space complexity via the spectral entropy of a survival (Loschmidt) amplitude for a fixed probe state $|\psi\rangle$,

$$C(t; \rho) = \langle \psi | e^{-iH(\rho)t} | \psi \rangle = \sum_n |c_n(\rho)|^2 e^{-iE_n(\rho)t}, \qquad c_n(\rho) = \langle E_n(\rho) | \psi \rangle. \tag{S20}$$

Let $S(\omega; \rho) = \left| \mathcal{F}[C(\cdot; \rho)](\omega) \right|^2$ be a windowed power spectrum and $P(\omega; \rho) = S(\omega; \rho) / \int S(\omega; \rho)\, d\omega$ its normalization. Let $\mathcal{F}$ denote the unitary Fourier transform in t, and

normalize $S(\omega)$ to a probability density $P(\omega)$ so that $\int P(\omega)\, d\omega = 1$. We then define

$$H_{\mathrm{spec}}(\rho) = -\int d\omega\, P(\omega;\rho)\, \ln P(\omega;\rho), \tag{S21}$$

which is small when a few frequencies dominate (coherent/locked motion) and large when many incommensurate frequencies carry comparable weights (dephasing and complex mixing). Peaks in $H_{\mathrm{spec}}(\rho)$ signal spectral broadening that typically accompanies a transition, followed by a drop once a new regime relocks the spectrum.

The linear response to the control parameter is captured by the free-energy curvature. With a linear deformation $H(\rho) = H_0 - \rho\,\hat{O}$ and $F(\rho) = -(1/\beta)\ln \mathrm{Tr}\, e^{-\beta H(\rho)}$,

$$F''(\rho) = \beta_{\mathrm{th}}\big(\langle \hat{O}^2\rangle - \langle \hat{O}\rangle^2\big), \qquad \beta_{\mathrm{th}} = 1/(k_{\mathrm{B}}T) \equiv \chi_O(\rho) \geq 0, \tag{S22}$$

and in the ground-state limit $F(\rho) \to E_0(\rho)$,

$$E_0''(\rho) = 2\sum_{n>0} \frac{|\langle n|\hat{O}|0\rangle|^2}{E_n(\rho) - E_0(\rho)}. \tag{S23}$$

Both formulas demonstrate enhancement by small gaps and large transition matrix elements; pronounced peaks in $F''(\rho)$ therefore locate parameter regions where the state is most sensitive to ρ.

The geometry of the projective Hilbert manifold is accessed through ground-state fidelity. Write $|\psi_0(\rho)\rangle$ for the normalized ground state of $H(\rho)$ with an arbitrary but fixed global phase convention.

$$F(\rho, \rho+\delta) = \big|\langle \psi_0(\rho) \mid \psi_0(\rho+\delta)\rangle\big| = 1 - \tfrac{1}{2}\,\chi_F(\rho)\,\delta^2 + O(\delta^3) \tag{S24}$$

defines the fidelity susceptibility

$$\chi_F(\rho) = \langle \partial_\rho\psi_0|\partial_\rho\psi_0\rangle - |\langle\psi_0|\partial_\rho\psi_0\rangle|^2 = \sum_{n>0} \frac{|\langle n|\hat{O}|0\rangle|^2}{\big(E_n(\rho) - E_0(\rho)\big)^2}. \tag{S25}$$

Sharp drops in F and peaks (or finite-size precursors thereof) in χ_F mark rapid ground-state reconfiguration, a hallmark of continuous transitions.

An additional dynamical diagnostic is the *maximum Lyapunov exponent* (MLE) $\lambda_{\max}(\rho)$, which quantifies the mean exponential divergence of nearby trajectories in the Lorenz flow itself. Writing $\delta x(t)$ for an infinitesimal perturbation that obeys the variational equation

$$\dot{\delta x}(t) = J(t;\rho)\,\delta x(t), \qquad J(t;\rho) = \frac{\partial f(x(t);\rho)}{\partial x} \tag{S26}$$

with $f = (\dot{x}, \dot{y}, \dot{z})$, one defines

$$\lambda_{\max}(\rho) = \lim_{t\to\infty} \frac{1}{t} \ln \frac{\|\delta x(t)\|}{\|\delta x(0)\|}, \tag{S27}$$

where the limit is realized numerically through periodic renormalization of $\delta x(t)$ in the Benettin algorithm. A negative $\lambda_{\max}$ indicates stable fixed points or periodic orbits, $\lambda_{\max} = 0$ corresponds to neutral stability at a bifurcation, and a positive $\lambda_{\max}$ indicates chaotic dynamics with exponential sensitivity to initial conditions. For the Lorenz parameters $(\sigma, \beta) = (10, 8/3)$, the computed $\lambda_{\max}(\rho)$ changes sign near $\rho_c \simeq 24.7$, in agreement with the classical onset of the strange attractor. This neighborhood has historically been described as a "preturbulent" regime in Lorenz-type flows (*67*). In our analysis, this transition in $\lambda_{\max}$ aligns closely with the peaks of spectral entropy and fidelity susceptibility, linking microscopic Hilbert-space sensitivity to macroscopic chaos in the underlying flow.

On the topological side, we examine loop robustness in the embedded attractor by persistent homology. The Vietoris–Rips filtration

$$R_\varepsilon(X(\rho)) = \{\sigma \subset X(\rho) : \max_{x,y\in\sigma} d(x,y) \le \varepsilon\} \tag{S28}$$

tracks H_1 classes through births b and deaths d; the persistence is $\ell = d - b$. We use the Euclidean metric $d(\cdot,\cdot)$ on the embedded point cloud $X(\rho)$, and the Rips complex includes a simplex whenever all pairwise distances within it are $\le \varepsilon$. As a compact summary we record the highest persistence

$$\ell_{H_1}^{\max}(\rho) = \max_i (d_i - b_i), \qquad Q_{\text{topo}}(\rho) = \frac{\ell_{H_1}^{\max}(\rho)}{1 + \ell_{H_1}^{\max}(\rho)} \in [0, 1), \tag{S29}$$

where large values indicate a clear, persistent loop (e.g., well-separated wings of the attractor), whereas kinks or drops versus ρ mark geometric reorganizations.

The same topological information admits a spectral representation through a supersymmetric (SUSY) Hamiltonian. Let the graded Hilbert space $\mathcal{H} = \bigoplus_k \mathcal{H}_k$ represent k–cochains, with $Q : \mathcal{H}_k \to \mathcal{H}_{k+1}$ the coboundary block d_k and $Q^\dagger$ its adjoint. The SUSY Hamiltonian $\mathcal{H}_{\mathrm{SUSY}} = \{Q, Q^\dagger\}$ is block-diagonal with

$$\mathcal{H}_{\mathrm{SUSY}}\big|_{\mathcal{H}_k} = d_k^\dagger d_k + d_{k-1} d_{k-1}^\dagger \;=\; \mathcal{L}_k, \tag{S30}$$

the combinatorial Hodge Laplacian. Zero-energy states satisfy $d_k v = 0$ and $d_{k-1}^\dagger v = 0$; hence,

$$\ker \mathcal{H}_{\mathrm{SUSY}}\big|_{\mathcal{H}_k} = \ker \mathcal{L}_k \cong H^k \text{ (and by duality } H_k), \qquad \dim \ker \mathcal{L}_k = \beta_k. \tag{S31}$$

For a self-adjoint matrix M, $\sigma(M)$ denotes its multiset of eigenvalues; $\min(\sigma(M) \setminus \{0\})$ is the first positive eigenvalue (if any).

$$\Delta_{\mathrm{SUSY}}^{(1)} = \min\{\lambda > 0 \mid \lambda \in \sigma(\mathcal{L}_1)\}. \tag{S32}$$

is a topological gap separating harmonic 1-cycles from their first excitations; its shrinkage (reopening) signals weakening (strengthening) of loop robustness and typically covaries with $\ell_{H_1}^{\max}(\rho)$.

If $\{E_n(\rho)\}_n$ denotes the ordered eigenvalues of $H(\rho)$, we define the many-body gap as $\gamma(\rho) = E_1(\rho) - E_0(\rho)$.

$$\gamma(\rho) = E_1(\rho) - E_0(\rho), \tag{S33}$$

which often obeys critical scaling near ρ_c,

$$\gamma(\rho) \sim |\rho - \rho_c|^{z\nu}, \qquad \xi(\rho) \sim |\rho - \rho_c|^{-\nu}, \qquad \gamma \sim \xi^{-z}, \tag{S34}$$

and, for linear size L (or an effective sample-size proxy),

$$\gamma(\rho, L) = L^{-z}\, \mathcal{F}\big((\rho - \rho_c) L^{1/\nu}\big), \qquad \gamma(\rho_c, L) \propto L^{-z}. \tag{S35}$$

In practice, the minima or closures of $\gamma(\rho)$ tend to align with the peaks of $F''(\rho)$ and $\chi_F(\rho)$ because of the small denominators in their spectral representations; at the same locations one often observes a peak in $H_{\mathrm{spec}}(\rho)$ and a kink or turnover in $\ell_{H_1}^{\max}(\rho)$ or $\Delta_{\mathrm{SUSY}}^{(1)}(\rho)$.

The experimental campaign thus evaluates the Lorenz system via ρ using both dynamical (spectral entropy, free-energy curvature, and fidelity) and topological (persistent H_1 and Hodge–Laplacian spectrum gaps) indicators, and it explores their physical significance jointly: spectral broadening and heightened response coincide with homology-carrying zero modes becoming weakly isolated. However, the relocking of frequencies and reduced susceptibility accompany the reopening of topological and spectral gaps. This consensus across indicators provides a robust locator of phase boundaries and a unified interpretation of dynamic and geometric reorganization in the Lorenz system.

S4 Pipeline Overview

The proposed framework transforms a real-valued time series into a quantum–mechanical spectral representation whose low-energy structure encodes the persistent topology of the underlying dynamics. By integrating classical topological data analysis (TDA) with quantum spectral estimation in a sequential and interpretable workflow, the method converts physical and geometric information into algebraic form, culminating in a supersymmetric (SUSY) Hamiltonian whose eigenvalue spectrum suggests homological features.

The end-to-end process comprises five main stages, illustrated schematically in Figure 1. First, a scalar observable from the Lorenz system is embedded into a reconstructed phase space via Takens' delay coordinates (Section S5). The resulting point cloud $X = \{X(t_k)\}$ approximates the invariant manifold of the attractor, preserving its loop topology and geometric structure.In particular, sliding-window constructions together with persistence have proven effective for extracting topological signatures from time-series data (*68*).

Next, a compact subset $V = \{v_i\}_{i=1}^{n}$ is extracted from X on the basis of density, topological persistence, and geometric diversity (Section S6). This topology-aware reduction retains the regions most relevant to persistent H_1 features while maintaining balanced spatial coverage. The selected representatives are then connected into an undirected graph $G = (V, E)$ that captures both local

geometric adjacency and dominant loop structures (Section S7). The edge set combines a minimum spanning tree backbone, a ε–neighborhood layer, and optional ring edges derived from circular coordinates obtained via persistent homology.

The graph's connectivity and topology are subsequently mapped onto a symmetric quantum probe state (Section S8). Weighted superpositions of Dicke states $|D_k^{(n)}\rangle$ encode local degrees, loop participation, and feature persistence in their excitation-number populations, ensuring compatibility with excitation-preserving SUSY dynamics.

Finally, from the constructed graph, we assemble a SUSY Hamiltonian $\mathcal{H} = Q^\dagger Q$ whose 1–form block $\mathcal{L}_1 = d_1^\dagger d_1 + d_0 d_0^\dagger$ acts as a discrete Hodge Laplacian on edges (Section S9). Its zero-energy kernel corresponds to the harmonic 1–cycles, whereas the first positive eigenvalue $\Delta_{\text{SUSY}}^{(1)}$ measures the spectral isolation of these topological features. The Hamiltonian is simulated via a controlled time-evolution circuit and probed through single-ancilla quantum phase estimation (QPE), yielding the low-lying energy spectrum.

This sequence may point toward a coherent mapping from temporal dynamics to quantum spectra: time series $\xrightarrow{\text{Takens embedding}}$ point cloud $\xrightarrow{\text{topology-aware reduction}}$ graph $G(V, E)$ $\xrightarrow{\text{SUSY encoding}}$ quantum Hamiltonian $\mathcal{H}$ $\xrightarrow{\text{QPE}}$ spectral features $\{\Delta_{\text{SUSY}}^{(k)}\}$. Each transformation—embedding, projection, graph construction, operator synthesis, and quantum measurement—preserves structural information while translating it across representations.

The classical components (embedding, sampling, and graph formation) compress continuous dynamics into discrete topological summaries, whereas the quantum components (state encoding, Hamiltonian simulation, and phase estimation) perform spectral inference without explicit matrix diagonalization, exploiting quantum parallelism for eigenvalue extraction. This hybrid approach combines interpretability from classical TDA with computational leverage from quantum simulation.

The main observables emerging from the pipeline include the low-lying eigenvalues $\{E_0, E_1, \dots\}$ of $\mathcal{H}$ and their spacing $\gamma = E_1 - E_0$, which quantify the dynamical spectral gap; the topological gap $\Delta^{(1)}_{\mathrm{SUSY}}$ from the 1–form block $\mathcal{L}_1$, which measures the robustness of persistent loops; the highest persistence $\ell^{\max}_{H_1}$ obtained from classical homology, which serves as a geometric benchmark, and the spectral entropy H_{spec} derived from the QPE amplitude distribution, which summarizes the frequency-space complexity. The correlations among these quantities reveal how dynamic and topological transitions interact under changes in the control parameter, such as the Rayleigh number ρ in the Lorenz flow.

By integrating geometric embedding, topological reduction, and quantum spectral estimation into a unified sequence, this framework provides a reproducible and physically interpretable route for detecting, characterizing, and quantifying topological signatures in nonlinear dynamics. The resulting hybrid representation enables both theoretical analysis and experimental realization of contemporary quantum hardware.

S5 Time series embedding

The first stage of the pipeline transforms a one-dimensional dynamical signal into a geometric representation suitable for topological and spectral analysis.

Following Takens' embedding theorem (*68–71*), the underlying attractor of the Lorenz flow is reconstructed from a scalar observable, producing a point cloud $X \subset \mathbb{R}^m$ that preserves the topology of the original state space appropriate simplicial complexes and reconstruction choices critically affect the recovered topology (*72*)..

The Lorenz system (*73–75*) is governed by

$$\dot{x} = \sigma(y - x), \qquad \dot{y} = x(\rho - z) - y, \qquad \dot{z} = xy - \beta z, \tag{S36}$$

with the canonical parameters $(\sigma, \beta, \rho) = (10,\ 8/3,\ 28)$ corresponding to the chaotic regime. This system generates a nonperiodic attractor of fractal dimension $\dim_H \approx 2.06$, which is sensitive to

initial conditions and a complex, folded topology. Varying the Rayleigh number ρ induces distinct dynamical phases, which are later examined through topological and spectral diagnostics.

From a single scalar measurement, for example, $x(t)$, we construct an m–dimensional delay-coordinate embedding,

$$X(t) = \left[x(t),\, x(t+\tau),\, x(t+2\tau),\, \ldots,\, x(t+(m-1)\tau)\right] \in \mathbb{R}^m, \tag{S37}$$

where τ is the time delay and m is the embedding dimension. Under generic smoothness and observability conditions, this mapping is diffeomorphic to the original attractor when $m > 2d_A$, where d_A denotes the attractor's dimension. The reconstructed manifold thus faithfully captures the invariant geometry of the flow.

The time delay τ controls the balance between redundancy and independence among coordinates. If τ is too small, consecutive components become nearly collinear, yielding an artificially thin manifold; if τ is too large, temporal correlation is lost, and attractor fragments are generated. Two practical selection rules are widely used: (i) choosing τ as the first minimum of the automutual information, which maximizes independence between coordinates, and (ii) setting τ to the $1/e$ decorrelation time of the autocorrelation function, which maintains dynamical coherence. For the Lorenz system, τ typically falls within $[0.05,\, 0.2]$ in dimensionless time units, producing stable embeddings with clearly separated loops.

The embedding dimension m must be large enough to unfold the attractor and prevent self-intersections, yet small enough to remain computationally manageable. In practice, m is increased until the fraction of false nearest neighbors (*76*) falls below a threshold (e.g., 1%) and the estimated correlation dimension (*77*) stabilizes. For the Lorenz flow, $m = 3$–6 typically suffices to recover the two-wing structure, whereas larger values further smooth sampling artifacts at the cost of redundancy.

To ensure numerical consistency across ρ, several safeguards are implemented. Initial transients of duration t_{trans} are discarded to eliminate sensitivity to initial conditions; integration of Eq. (S36)

is performed with a fixed time step Δt to prevent stiffness-induced distortions; trajectories are downsampled so that the sampling stride is comparable to τ, avoiding oversampling of correlated points; and each coordinate is normalized to unit variance before distance calculations. These procedures maintain numerical stability and geometric consistency over parameter sweeps (*78, 79*).

The quality of the embedding is verified by estimating the largest Lyapunov exponent $\lambda_{\max}$ from the reconstructed series (*80–82*). A positive $\lambda_{\max}$ is consistent with the reconstructed dynamics preserving the expected chaotic character. Additionally, visual inspection of the attractor projection and its persistence diagram ensures that characteristic topological features—such as the double-wing loop—remain intact.

The embedding yields a point cloud

$$X = \{X(t_k) \in \mathbb{R}^m\}_{k=1}^{N}, \tag{S38}$$

which samples the invariant manifold of the Lorenz attractor. Euclidean distances $\|X_i - X_j\|_2$ capture local dynamical adjacency and form the geometric substrate for subsequent topological and spectral analyses. This point cloud provides the input for the representative-point selection step (Section S6), where density, topology, and diversity criteria are applied to extract a compact but faithful subset of points.

Under the selected (τ, m), the Lorenz embedding produces a cloud whose Vietoris–Rips filtration results in two persistent H_1 classes corresponding to the attractor's wings, which is consistent with previous studies (*83, 84*). These structures are stable across time windows and parameter variations, confirming that the embedding serves as a robust precursor for quantum–topological encoding.

Takens embedding therefore transforms a scalar chaotic signal into a geometric object that retains the essential topology of the underlying flow. The appropriate choices of τ and m, combined with numerical safeguards, ensure that the resulting point cloud faithfully represents the attractor's loop geometry. This embedded manifold forms the geometric foundation upon which topology preserving reduction and supersymmetric Hamiltonian encoding are subsequently built.

S6 Representative Point Selection

Given an embedded point cloud $X = \{x_i \in \mathbb{R}^m\}_{i=1}^N$, the task is to extract a smaller subset of representative points $V = \{v_j\}_{j=1}^n$ ($n \ll N$) that preserves the high-density regions of the attractor, the essential loop topology captured by persistent H_1, and the overall geometric diversity of the data. This reduction yields a tractable input for graph and Hamiltonian construction while maintaining the topological integrity of the system.

The selection process proceeds in two main stages. In the first stage, topology-aware sampling identifies regions supporting persistent H_1 features and high local density. Second, a complementary set of points is added to maximize the geometric spread, ensuring that the global features and sparse regions are not neglected. The combination produces a compact yet topology-preserving representative set V.

Let $D(x, y) = \|x - y\|_2$ denote the Euclidean distance, and let k be the target number of representatives. A fraction $r \in (0, 1)$ of these, $k_{\text{topo}} = \lfloor kr \rfloor$, is reserved for topological coverage, with the remaining $k_{\text{global}} = k - k_{\text{topo}}$ used for global diversity. A K-nearest-neighbor (KNN) graph (typically $K \approx 10$) is constructed on X, and its shortest-path metric D_{geo} approximates geodesic distance along the manifold.

The local density is estimated via a Gaussian kernel:

$$\rho(x_i) = \frac{1}{N\, h^m} \sum_{j=1}^{N} \exp\Big(- \frac{\|x_i - x_j\|^2}{2h^2} \Big), \tag{S39}$$

where the bandwidth h is chosen as the 10th percentile of pairwise distances to ensure robustness against outliers. Positive weights are then defined as

$$w_i \propto \rho(x_i)^{\,\alpha - 1}, \qquad \alpha > 1, \tag{S40}$$

so that dense regions exert a stronger influence on the selection.

To identify points most relevant to loop topology, the Vietoris–Rips persistent homology of X is computed and the most persistent H_1 feature with birth–death pair (b^*, d^*) is located. Its midpoint radius is

$$r_{\text{mid}} = \tfrac{1}{2}(b^* + d^*), \tag{S41}$$

sets a characteristic neighborhood scale. For each point x_i, the mid-scale neighbor count

$$\nu_i = \#\{\, j : D(x_i, x_j) < r_{\text{mid}} \,\} \tag{S42}$$

quantifies local crowding at that scale. Points with excessively few or many neighbors are excluded by defining the candidate set

$$I = \left\{ i \,\middle|\, N_{\min} < \nu_i < N_{\max} \right\}, \quad N_{\min} \approx \lfloor 0.02N \rfloor, \quad N_{\max} \approx \max\{N_{\min}{+}5, \lfloor 0.10N \rfloor\}. \tag{S43}$$

When a dominant H_1 loop is present, each point x_i is assigned an angular coordinate $\theta_i \in [0, 2\pi)$ derived from persistent cohomology circular coordinates. The interval $[0, 2\pi)$ is discretized into B bins to encourage uniform angular sampling around the loop.

The topological subset S_{topo} is initialized with the point of maximal density weight $w_i^{\alpha-1}$ within I. While $|S_{\text{topo}}| < k_{\text{topo}}$, new points are added greedily by maximizing the composite gain function

$$\Delta(j) = \lambda_\theta \, \Delta H_\alpha(h \oplus \theta_j) + \lambda_D \min_{i \in S_{\text{topo}}} D_{\text{geo}}(x_j, x_i) + \lambda_d \, H_\alpha\big(\{q_i\}_{i \in S_{\text{topo}} \cup \{j\}}\big) - \lambda_c \, \Pi(\theta_j \mid \{\theta_i\}_{i \in S_{\text{topo}}}), \tag{S44}$$

where H_α is the Rényi entropy, $q_i \propto \rho(x_i)$ are normalized density weights, $\Delta H_\alpha(h \oplus \theta_j)$ measures the entropy gain from adding θ_j to the angular histogram, and Π penalizes violations of a minimum angular separation $\Delta\theta_{\min} \approx 2\pi/(1.35\, k_{\text{topo}})$. The hyperparameters $(\lambda_\theta, \lambda_D, \lambda_d, \lambda_c)$ balance angular diversity, geodesic spacing, density regularization, and collision avoidance. This greedy procedure incrementally increases coverage of the loop while maintaining separation and balance.

Once the topological representatives are chosen, the remaining k_{global} points are selected to maximize global diversity. For each unselected candidate, its minimum distance from the topological

set is defined as

$$d_{\min}(x_j) = \min_{i \in S_{\text{topo}}} D(x_j, x_i), \tag{S45}$$

and a combined score

$$\text{score}(x_j) = w_j \cdot (1 + d_{\min}(x_j)) \tag{S46}$$

is computed to prioritize dense but distant regions. The highest-scoring points are successively added to form the global coverage set S_{global}.

The final representative set is the union

$$V = S_{\text{topo}} \cup S_{\text{global}}, \qquad |V| = k. \tag{S47}$$

The parameters $(r, \alpha, h, B, \lambda_\theta, \lambda_D, \lambda_d, \lambda_c)$ collectively govern the trade-off between density preservation, loop fidelity, and geometric spread. For Lorenz-type attractors, empirical tests show that r values between 0.5 and 0.7 provide a stable balance.

The resulting representative points are concentrated near persistent cycles and bridge regions of high Betti stability, while the globally selected points capture the outer geometry and noncyclic regions. Together, they yield a compact and faithful summary of the attractor's structure, substantially reducing the matrix dimensions for subsequent Laplacian and SUSY Hamiltonian construction without sacrificing the accuracy of homological inference.

In terms of computational cost, density estimation scales as $O(N^2)$ (reducible with KD-tree or approximate-nearest-neighbor acceleration), persistent homology scales as $O(N^{3/2})$ for typical point cloud, and greedy selection scales as $O(k^2)$. The only sources of stochasticity are tie-breaking and angular-bin initialization, which can be controlled by fixing the random seed to ensure reproducibility. The resulting set V provides the foundation for the topological edge construction described in Section S7.

S7 Topological Edge Construction

Given a reduced representative point set $V = \{v_i\}_{i=1}^{n} \subset \mathbb{R}^m$, the objective is to construct an undirected graph $G = (V, E)$ that preserves local geometric proximity, remains globally connected, and exposes prominent one-dimensional cycles when they exist. This graph functions as the 1–skeleton of a simplicial complex whose Hodge Laplacian encodes the persistent H_1 topology of the data.

To achieve this, the edge set E must capture both geometric adjacency and topological evidence. We combine a global backbone built from a minimum spanning tree (MST), a local neighborhood layer derived from an ε–graph, and an optional ring augmentation guided by circular coordinates. The resulting union is patched to ensure single-component connectivity, yielding a sparse yet expressive graph that reflects both metric and topological structure.

We begin with the pairwise distance matrix $D_{ij} = \|v_i - v_j\|_2$, from which the MST outlines a baseline connectivity without redundant long edges:

$$E_{\mathrm{MST}} = \arg \min_{T \subseteq \binom{V}{2}, |T|=n-1} \sum_{(i,j)\in T} D_{ij}. \tag{S48}$$

This minimal tree ensures that G is connected and acyclic, providing a global scaffold upon which additional edges can be added to recover the local structure.

The local geometry is then restored by introducing edges shorter than a data-driven threshold ε. Let $U = \{D_{ij} : 1 \le i < j \le n\}$ be the multiset of pairwise distances. A robust length scale is set as the 30th percentile, $\varepsilon = Q_{0.3}(U)$, and all pairs satisfying

$$E_\varepsilon = \{(i, j) : D_{ij} < \varepsilon\} \tag{S49}$$

are connected. This ε–graph preserves local neighborhoods and manifold adjacency while avoiding excessive long-range links, thereby restoring the short-range curvature fidelity that the MST alone omits.

When persistent homology suggests a strong H_1 signal, we further augment the structure by explicitly forming a ring that reinforces the dominant loop. Each vertex v_i is assigned an angular coordinate $\theta_i \in [0, 2\pi)$ obtained from persistent cohomology, spectral embedding, or a surrogate PCA–atan2 projection. Sorting the subset $V_{\text{ring}} \subseteq V$ by θ_i, we connect consecutive points with wrap-around closure:

$$E_{\text{ring}} = \left\{(i_k, i_{k+1})\right\}_{k=1}^{|V_{\text{ring}}|-1} \cup \{(i_{|V_{\text{ring}}|}, i_1)\}, \tag{S50}$$

embedding an explicit cycle corresponding to the most persistent homology class. If no significant H_1 feature is detected, this augmentation is omitted.

The provisional edge set,

$$E' = E_{\text{MST}} \cup E_\varepsilon \cup E_{\text{ring}}, \tag{S51}$$

may still contain multiple connected components, especially when the representative points occupy disjoint or sparsely sampled regions. To restore global connectivity, we iteratively link components by adding the shortest intercomponent edge,

$$(i^\star, j^\star) = \arg \min_{i \in C_p,\, j \in C_{p+1}} D_{ij}, \tag{S52}$$

until a single connected graph remains. The added edges form the patch set E_{patch}.

The final edge collection is thus

$$E = E_{\text{MST}} \cup E_\varepsilon \cup E_{\text{ring}} \cup E_{\text{patch}}, \tag{S53}$$

ensuring that $G = (V, E)$ is connected, locally faithful, and topologically expressive. Edges from the MST enforce global reachability; those from E_ε reconstruct local geometry; and those from E_{ring} explicitly embed the dominant one-dimensional cycle. Together, these elements guarantee that the cycle space $\ker B_1$ of G accurately reflects the principal H_1 feature of the attractor. For loop-like geometries such as the Lorenz double-wing attractor, ring augmentation ensures that the first Betti number $\beta_1 = 1$ is preserved in the graph Laplacian $L_1 = B_1^\top B_1$ before supersymmetric extension.

The quantile threshold $Q_{0.3}$ can be tuned to data density: higher quantiles increase local connectivity but risk introducing spurious short cycles, whereas lower values may fragment the graph. Both ε and MST edges are computed via Euclidean distances for stability, although alternative metrics such as geodesic or diffusion distances may be substituted. Deterministic tie-breaking is applied in (S48) and (S52) to ensure reproducibility.

The computational cost of each step scales efficiently: MST construction requires $O(n \log n)$ via Kruskal or Prim algorithms, the ε–graph formation scales as $O(n^2)$ (or $O(n \log n)$ with spatial indexing), and the ring augmentation scales linearly with $|V_{\text{ring}}|$. The final graph contains $O(n)$ edges in typical sparse settings, making it tractable for both classical Laplacian assembly and quantum operator encoding (Section S9). All subsequent SUSY Hamiltonian blocks $\mathcal{L}_k$ inherit this sparsity, enabling efficient simulation via product-formula time evolution.

The constructed graph G therefore acts as a compact, topology-aware skeleton of the embedded attractor. It faithfully preserves local neighborhoods while revealing the main loop structure identified by persistent homology. This balance between geometric fidelity and topological simplicity is crucial for ensuring that the SUSY Hamiltonian derived from G accurately encodes the persistent H_1 features in its low-energy spectrum.

S8 Dicke State Encoding

The aim is to encode the topology of the representative-point graph into a quantum probe that predominantly resides in the symmetric subspace of $(\mathbb{C}^2)^{\otimes n}$. Dicke states form a natural and computationally efficient basis for this purpose: they capture global excitation-number symmetry, preserve combinatorial structure, and admit compact circuit representations with logarithmic depth. For n qubits, the weight-k Dicke state is

$$|D_k^{(n)}\rangle = \binom{n}{k}^{-1/2} \sum_{\substack{x \in \{0,1\}^n \\ |x|=k}} |x\rangle\,, \qquad k = 0, 1, \ldots, n, \tag{S54}$$

where $\{|x| = k\}$ is the set of computational strings of Hamming weight k. These states are orthonormal and span the $(n{+}1)$-dimensional symmetric subspace $\mathcal{H}_{\mathrm{sym}}$, diagonalizing the collective spin $J_z = \frac{1}{2}\sum_{i=1}^{n} Z_i$ with eigenvalues $m_k = k - \frac{n}{2}$. Throughout, we use the ordering $|x\rangle = |x_{n-1}\ldots x_0\rangle$ and the subset index $\mathrm{ind}(S) = \sum_{i\in S} 2^i$ for $S \subseteq \{0,\ldots,n-1\}$, so that amplitudes are assigned uniformly within each weight-k sector, and normalization ensures $\langle D_k^{(n)}|D_{k'}^{(n)}\rangle = \delta_{kk'}$.

The topological information extracted from the graph $G = (V, E)$ is embedded into a symmetric superposition of Dicke sectors:

$$|\psi\rangle = \frac{\sum_{k=0}^{n} \tilde{w}_k \; |D_k^{(n)}\rangle}{\left\| \sum_{k=0}^{n} \tilde{w}_k \; |D_k^{(n)}\rangle \right\|}, \qquad \tilde{w}_k = \frac{w_k}{\sqrt{\sum_j w_j^2}}, \tag{S55}$$

where the unnormalized weights w_k encode both local connectivity and global loop persistence. Local bias arises from degrees and ring participation: letting $\mathcal{E}_{\mathrm{ring}}$ denote edges that lie on the dominant cycle and $\deg(v)$ the degree of vertex v, the update

$$w_k \;\leftarrow\; w_k \;+\; \alpha \sum_{(u,v)\in\mathcal{E}_{\mathrm{ring}}} \Big[\mathbf{1}\{u = k\} + \mathbf{1}\{v = k\}\Big] \;+\; \beta \sum_{v:\deg(v)=k} 1 \tag{S56}$$

reinforces sectors touched by the ring and emphasizes hubs, with tunable $\alpha, \beta \geq 0$ setting the relative importance of the two contributions. Global topological strength further modulates contrast via the persistence Λ of the most persistent H_1 class:

$$w_k \;\leftarrow\; (1 + \eta\,\Lambda)\, w_k, \qquad \eta > 0, \tag{S57}$$

which amplifies all sectors proportionally when a robust loop is present while preserving the local bias profile.

After normalization, sector populations $p_k = |\langle D_k^{(n)}|\psi\rangle|^2 = \tilde{w}_k^{\,2}$ define a probability distribution over the excitation number. The expectation

$$M = \sum_k \big(k - \tfrac{n}{2}\big)\, p_k = \langle\psi|J_z|\psi\rangle \tag{S58}$$

plays the role of a magnetization-like order parameter, and the variance $\mathrm{Var}(J_z) = \sum_k (k - \frac{n}{2} - M)^2 p_k$ yields the quantum Fisher information $F_Q = 4\,\mathrm{Var}(J_z)$, linking the breadth of the excitation

distribution to metrological sensitivity. In this way, loop prominence and heterogeneity manifest as broadening of $\{p_k\}$, nonzero M, and enhanced F_Q, providing a direct statistical signature of topological complexity.

Crucially, the supersymmetric Hamiltonian $\mathcal{H}$ constructed in Section S9 conserves the total excitation number and decomposes into blocks $\mathcal{L}_k$ acting on the weight-k sector:

$$e^{-i\mathcal{H}t} = \bigoplus_{k=0}^{n} e^{-i\mathcal{L}_k t}. \tag{S59}$$

A probe of the form (S55) therefore aligns with the block-diagonal structure of $\mathcal{H}$ and maximizes overlap with homology-bearing low-energy modes. Because the excitation number is conserved, evolution remains within the symmetric manifold—significantly reducing the Hilbert space dimension from 2^n to $(n+1)$ and thereby lowering the simulation and QPE circuit costs. The single-ancilla Hadamard test or QPE then accesses the autocorrelation

$$C(t) = \langle\psi|e^{-i\mathcal{H}t}|\psi\rangle = \sum_k p_k\, e^{-iE_k t}, \tag{S60}$$

whose spectral lines at $\{E_k\}$ expose near-harmonic modes tied to topological features while preserving the symmetric-sector decomposition.

The implementation of near-term hardware requires exact or approximate preparation. Exactly $|D_k^{(n)}\rangle$ states can be synthesized in logarithmic depth via permutation-symmetric isometries or tree networks of controlled rotations; approximate preparation is achievable with variational or iterative amplitude-loading schemes. The superposition $\sum_k \tilde{w}_k\, |D_k^{(n)}\rangle$ is realized by preparing a weight register and mapping $|k\rangle\,|0^n\rangle \mapsto |k\rangle\,|D_k^{(n)}\rangle$, followed by uncomputing $|k\rangle$; normalization of $\{\tilde{w}_k\}$ stabilizes amplitudes numerically. Because the excitation number is conserved under $e^{-i\mathcal{H}t}$, there is no cross-sector leakage during evolution, which simplifies the controlled time evolution and reduces the circuit depth in the QPE.

From a physical standpoint, graphs with balanced connectivity concentrate weights near $k \simeq n/2$, yielding $M \simeq 0$ and narrower distributions; sparse or strongly cyclic graphs skew $\{p_k\}$, induce

nonzero magnetization, and increase F_Q. The Dicke manifold thus provides an interpretable encoding in which loop geometry and symmetry breaking translate into measurable sector populations and interferometric sensitivity. In summary, Dicke-state encoding turns the classical H_1 structure into structured superpositions across excitation-number sectors, couples naturally to the SUSY block structure, and yields a probe that is both conceptually transparent and hardware-efficient for quantum spectral readout.

While the Dicke-state formalism provides a compact theoretical description, exact preparation of $|D_k^{(n)}\rangle$ on current devices remains resource-intensive. In our implementation, we employed a simplified circuit that efficiently generates the single-excitation (k=1) Dicke state $|W_n\rangle = |D_1^{(n)}\rangle$ from $|100\ldots0\rangle$ via a linear sequence of controlled-R_y and CNOT gates. This scheme transfers the excitation along the register, dividing the amplitude evenly at each step and achieving depth $O(n)$ while maintaining high fidelity under realistic noise. Higher-weight sectors are then approximated by composing multiple W-state layers or by variational amplitude-loading when available. Thus, although the analytical description uses the full Dicke manifold, the experimental embedding adopts an optimized, hardware-compatible version that retains the essential symmetry and spectral features relevant to the QPE readout.

S9 SUSY Hamiltonian Construction

The supersymmetric Hamiltonian $\mathcal{H}$ is constructed on n qubits to faithfully encode the topology of the representative-point graph $G = (V, E)$ obtained from the data. The operator is designed to obey the $\mathcal{N} = 2$ supersymmetry algebra, preserve the excitation number, and remain efficiently simulable on quantum hardware. The SUSY Hamiltonian coincides with the combinatorial Hodge–Laplacian. In particular, the zero-energy sector encodes topological invariants of the graph, such as the Betti numbers.

We define the following local operators that act on each qubit:

$$\{I, X, Z,\ z, o\}, \qquad z = \tfrac{I+Z}{2},\ \ o = \tfrac{I-Z}{2}, \tag{S61}$$

where z and o act as projectors onto $|0\rangle$ and $|1\rangle$, respectively. All the local letters are Hermitian and real, and after Hermitization, the Hamiltonian $\mathcal{H}$ becomes real and symmetric. The set $\{I, X, Z, z, o\}$ is sufficient for representing the Projected-basis SUSY Hamiltonian without introducing complex Y rotations.

Fermionic excitations are represented by Jordan–Wigner strings that ensure proper anticommutation. For vertex i, the elementary flip operator is

$$X_i^{\mathrm{JW}} = \Big(\prod_{k<i} Z_k\Big) X_i. \tag{S62}$$

To enforce clique consistency, we introduce complement-graph projectors. For each vertex i, let

$$N_i^{\mathrm{comp}} = \{j \in V : (i, j) \notin E,\ j \neq i\}, \tag{S63}$$

and define

$$P_i = \prod_{j \in N_i^{\mathrm{comp}}} \frac{I + Z_j}{2} = \bigotimes_{j \in V} \begin{cases} z_j, & j \in N_i^{\mathrm{comp}}, \\ I_j, & \text{otherwise.} \end{cases} \tag{S64}$$

These projectors annihilate configurations in which vertex i is excited simultaneously with a nonneighbor, enforcing adjacency constraints. The elementary supercharge at site i is $Q_i = X_i^{\mathrm{JW}} P_i$, and the total supercharge is $Q = \sum_i Q_i$, and by construction $Q^2 = 0$.

The Hamiltonian functions as the anticommutator

$$\mathcal{H} = Q^\dagger Q = \sum_i Q_i^\dagger Q_i + \sum_{i<j} (Q_i^\dagger Q_j + Q_j^\dagger Q_i), \tag{S65}$$

which automatically commutes with the excitation number. In the 0–excitation sector, $\mathcal{H}$ acts as the vertex Laplacian $\mathcal{L}_0$; in the 1–excitation sector, $\mathcal{H}$ acts as the edge Laplacian $\mathcal{L}_1$; and in higher sectors,$\mathcal{H}$ acts as clique Laplacians for multiexcitation configurations:

$$\mathcal{H} = \bigoplus_{k=0}^{n} \mathcal{L}_k, \qquad \mathcal{L}_k = d_k^\dagger d_k + d_{k-1} d_{k-1}^\dagger. \tag{S66}$$

This block decomposition mirrors the combinatorial Hodge structure and ensures correspondence between harmonic subspaces and homology groups.

Substituting the operator definitions,

$$z = \tfrac{I+Z}{2}, \quad o = \tfrac{I-Z}{2}, \tag{S67}$$

clarifies that each local factor belongs to the $\{I, X, Z\}$ Pauli family and that z, o act only as symbolic projectors composed of them. In practice the full (I, Z) expansion of z, o is not carried out; they are treated as diagonal control predicates. Under this symbolic treatment, $\mathcal{H}$ remains a sparse sum of few-qubit Pauli operators with real coefficients.

Because each supercharge Q_i acts nondiagonally on a single qubit and diagonally (via projectors) on the rest, the interaction structure involves only qubit pairs (i, j) that share an edge in G. For graphs of bounded degree, the number of distinct tensor-product terms therefore scales quadratically in n, $O(n^2)$, rather than exponentially in 4^n. This estimate has been verified for the representative Lorenz-derived graphs used here, where the compiled Hamiltonians contain a few hundred terms. After Hermitization, the operator is real and symmetric.

The kernel of $\mathcal{H}$ corresponds to harmonic forms:

$$\ker \mathcal{H}\big|_{k-\text{sector}} = \ker \mathcal{L}_k \cong H^k, \tag{S68}$$

so that the multiplicity of zero eigenvalues in degree 1 equals the first Betti number β_1. The smallest nonzero eigenvalue,

$$\Delta^{(1)}_{\text{SUSY}} = \min\{\lambda > 0 \mid \lambda \in \sigma(\mathcal{L}_1)\}. \tag{S69}$$

acts as a *topological gap* that measures the spectral isolation of persistent cycles, as formally justified in the Supplementary Materials (Section S12). Its variation with the control parameter ρ tracks the emergence, merger, and decay of topological features.

Any global energy offset $c_I I$ appearing in the Pauli expansion is separated as $\mathcal{H} = c_I I + (\mathcal{H} - c_I I)$, with phase $c_I t$ applied only to the ancilla branch during controlled evolution. This adjustment stabilizes interferometric measurements while leaving the eigenvectors and relative gaps intact.

For simulation, each exponential $e^{-i\theta t \bigotimes_q P_q}$ is implemented by reducing local letters to Z, aggregating parity with CNOT ladders, and applying a controlled $R_Z(2\theta t)$ on the reference qubit conditioned on the predicate. Because the complement-graph projectors commute, control masks can be toggled efficiently in Gray order (*85*) so that successive terms differ by a single-qubit flip. Grouping identical Pauli-letter patterns consolidates many rotations into a single R_Z, and multicontrol conjunctions are computed into an ancilla bit, replacing deep multicontrolled gates with two MCX operations and one CR_Z operation.

The resulting Hamiltonian is sparse, local, and block-diagonal, explicitly preserving topological sectors (*15*). For typical Lorenz-derived graphs ($n \approx 10$–12), the compiled operator contains a few hundred Pauli strings and fewer than 10^3 controlled rotations, well within the current simulator and NISQ capabilities. The method extends naturally to higher spatial dimensions by including multiple excitation constraints, providing a scalable template for encoding combinatorial Laplacians as quantum circuits.

This Hamiltonian reproduces the spectral structure of the Hodge Laplacian; its low-lying gaps empirically covary with persistent-Laplacian features. In this way, the SUSY Hamiltonian serves as an algebraic bridge between discrete topological data analysis and measurable quantum spectra, enabling topological invariants to be extracted directly through quantum phase estimation.

S10 Controlled Time Evolution Circuit

For quantum phase estimation on a supersymmetric Hamiltonian $\mathcal{H}$, we synthesize the ancilla-controlled time evolution

$$U_{\text{ctrl}}(t) = |0\rangle\langle 0| \otimes I + |1\rangle\langle 1| \otimes e^{-i\mathcal{H}t}, \tag{S70}$$

Thus, interference between the ancilla and system registers encodes the spectral phase of $\mathcal{H}$ with high fidelity (*48, 86, 87*). The construction proceeds term by term and is illustrated in Figure S1 and Figure S2, whereas the Gray-order traversal used to optimize control toggles is shown in Figure S3.

Each local factor of $\mathcal{H}$ is drawn from the symbolic alphabet

$$\{I, X, Z, z, o\}, \qquad z = \tfrac{I+Z}{2}, \quad o = \tfrac{I-Z}{2},$$

so that

$$\mathcal{H} = \sum_{\ell} \theta_\ell \bigotimes_{q=1}^{n} P_q^{(\ell)}, \qquad P_q^{(\ell)} \in \{I, X, Z, z, o\}, \tag{S71}$$

with real coefficients $\mathrm{Re}(\theta_\ell)$ after Hermitization. Each term acts on a small subset of qubits, ensuring sparsity and locality (*15, 88*). For a local operator $\mathcal{H}_\ell = \theta_\ell \bigotimes_{q\in S_\ell} P_q^{(\ell)}$, the rightmost active qubit $r = \max S_\ell$ serves as the reference site. To standardize all the terms, the nondiagonal operators are converted to Z form via a Hadamard gate on each affected qubit, as depicted in the left half of Figure S2. In the present construction, all off-diagonal couplings originate from X-type flip terms in the supercharges. The Y operator does not appear because no complex phase rotations are required; all the coefficients are real after Hermitization.

After basis alignment, a CNOT ladder

$$L_\ell = \prod_{q\in S_\ell \setminus \{r\}} \mathrm{CNOT}(q \to r) \tag{S72}$$

collects the parity of all Z factors onto the reference qubit (*89*), ensuring $L_\ell^\dagger\big(\prod_{q\in S_\ell} Z_q\big)L_\ell = Z_r$. The controlled evolution for that term then reduces to a single $R_Z(2\,\mathrm{Re}(\theta_\ell)t)$ rotation on qubit r, conditioned on the ancilla and any projector controls. The right halves of Figure S1 and Figure S2 show this structure: parity is gathered on r, the ancilla-controlled rotation applies the phase, and all intermediate operations are uncomputed to restore the original basis.

Projector symbols $z = (I+Z)/2$ and $o = (I-Z)/2$ correspond to $|0\rangle$- and $|1\rangle$-controls, respectively. To unify them, temporary X gates toggle $|0\rangle$-controls into the $|1\rangle$ basis, and a multiqubit conjunction is computed into an auxiliary predicate qubit,

$$\Pi_\ell = \mathrm{AND}\big(\text{ancilla},\, C_0^{(\ell)},\, C_1^{(\ell)}\big), \tag{S73}$$

where *ancilla* denotes the interference qubit used in the Hadamard-test or the QPE protocol. It is initialized in $(|0\rangle + |1\rangle)/\sqrt{2}$ and controls whether the system register undergoes time evolution: the

$|0\rangle$ branch remains idle, whereas the $|1\rangle$ branch activates the controlled evolution $e^{-i\mathcal{H}t}$. The sets $C_0^{(\ell)}$ and $C_1^{(\ell)}$ index the projector-controlled qubits associated with z- and o-type predicates, respectively. The composite predicate Π_ℓ therefore represents the logical AND of all active controls—ancilla, $|0\rangle$-controls, and $|1\rangle$-controls—and acts as a single effective control (*90, 91*) for the rotation gate.

Each local exponential term is then written as

$$U_\ell(t) = U_\mathrm{b}\, U_\mathrm{lad} \left[R_Z(2\,\mathrm{Re}(\theta_\ell)t) \text{ on qubit } r \text{ controlled by } \Pi_\ell \right] U_\mathrm{lad}^\dagger U_\mathrm{b}^\dagger, \tag{S74}$$

where U_b collects the basis transformations (e.g., H or $R_x(-\pi/2)$ rotations), and U_lad is the *CNOT ladder* circuit that aggregates the parity of all Z-type factors onto the rightmost active qubit $r = \max S_\ell$ before the controlled rotation.

This construction ensures that each local factor $\bigotimes_{q\in S_\ell} P_q^{(\ell)}$ is implemented with minimal control overhead while preserving the full commutation structure.

Since all R_Z rotations commute, terms sharing the same control mask and reference qubit can be merged. To minimize the number of control toggles between successive terms, the control masks are scheduled in Gray order, as shown in Figure S3, where consecutive masks differ by only a single bit. Predicate caching further lowers the depth by computing the logical AND once, applying one CR_Z, and uncomputing it.

The total time evolution over duration t is approximated via product formulas (*15, 88*). A first-order Trotter step

$$\tilde{U}_1(t) = \prod_\ell U_\ell(t)$$

achieves $O(t^2)$ accuracy, whereas the symmetric second-order step

$$\tilde{U}_2(t) = \tilde{U}_1(t/2)\, \tilde{U}_1(-t/2)^\dagger$$

suppresses the error to $O(t^3)$, with the bound

$$\left\| e^{-i\mathcal{H}t} - \tilde{U}(t) \right\| = O\left(t^2 \max_{\ell,\ell'} \| [\mathcal{H}_\ell, \mathcal{H}_{\ell'}] \| \right).$$

A global energy offset $\mathcal{H} = c_I I + (\mathcal{H} - c_I I)$ is handled by applying $e^{-ic_I t}$ only to the ancilla's $|1\rangle$ branch, stabilizing the interferometric phase without affecting the eigenvectors or relative gaps.

After grouping and optimization, the circuit depth is dominated by a few parity ladders and multicontrol rotations, whereas most remaining operations are commuting single-qubit R_Z gates. For typical systems with $n \approx 10$ qubits, a complete controlled evolution requires $\sim 10^4$ primitive gates. Gray-ordered scheduling and commuting-group compilation reduce entangling depth by a factor of 3–5 while maintaining spectral fidelity at the 10^{-3} level in the extracted gap γ. The resulting construction provides an efficient and hardware-compatible realization of $U_{\mathrm{ctrl}}(t)$ suitable for Hadamard-test and QPE-based spectroscopic estimation of supersymmetric energy gaps (*28, 92*).

This Projected-basis compilation not only reduces the circuit depth but also emulates the structural evolution of the combinatorial Laplacian under topological filtration. As noted in the persistent spectral framework of Meng and Xia (*93*), the number and strength of off-diagonal Laplacian entries vary systematically as simplices are added or removed along a filtration, producing a continuous growth and decay of coupling terms that governs spectral transitions. In our implementation, the Projected-basis realizes this mechanism at the operator level: Pauli-grouped commuting terms encode diagonal potentials, whereas Projected-basis operations selectively activate or suppress off-diagonal couplings corresponding to newly formed or annihilated simplices. Consequently, the controlled time-evolution operator $U(t) = e^{-i\widetilde{\mathcal{H}}t}$ mimics the dynamic modulation of connectivity observed in persistent Laplacian models, ensuring that the evolution of the quantum spectrum reproduces the same addition–removal process of Laplacian couplings that drives the filtration-dependent spectra.

S11 Quantum phase estimation (eigenvalue extraction)

We recover the eigenvalues of the supersymmetric Hamiltonian $\mathcal{H}$ by analysing the time autocorrelation of a prepared probe state. For a normalized state $|\psi\rangle$, the correlation function is

$$C(t) = \langle\psi|e^{-i\mathcal{H}t}|\psi\rangle = \sum_j a_j e^{-iE_j t}, \qquad a_j = |\langle E_j|\psi\rangle|^2, \;\; a_j \geq 0, \; \sum_j a_j = 1, \tag{S75}$$

so that the frequency content consists of spectral lines at $\{E_j\}$ with nonnegative weights $\{a_j\}$. The measurement is performed via a single-ancilla Hadamard test (Figure S4): the ancilla prepares $(|0\rangle+|1\rangle)/\sqrt{2}$, interferes with a reference branch with a data branch undergoing controlled evolution $e^{-i\mathcal{H}t}$, and is measured along X or Y, yielding $\langle X\rangle = \Re\, C(t)$ and $\langle Y\rangle = -\,\Im\, C(t)$. The correlation function $C(t)$ is sampled on a uniform grid $t_k = k\,\Delta t$ for $k = 0, \ldots, T-1$. Identity offsets are removed by writing $\mathcal{H} = c_I I + (\mathcal{H} - c_I I)$ and applying the global phase $e^{-ic_I t}$ only to the ancilla's $|1\rangle$ branch, so that the measured phases reflect $\mathcal{H} - c_I I$.

Because the Hadamard test measures the expectation value $\mathrm{Tr}(\rho\, e^{-i\mathcal{H}t})$ for an arbitrary density operator ρ, the same circuit applies without modification to statistical mixtures or decohered superpositions. In practice, we emulate such mixedness by averaging over random single–qubit Z phases within the Hadamard–test loop, effectively transforming $\rho = |\psi\rangle\langle\psi|$ into $\rho = \mathbb{E}_Z[Z|\psi\rangle\langle\psi|Z^\dagger]$ and suppressing off–diagonal coherences between Dicke sectors. In particular, for the Dicke–encoded probe $\rho = \sum_k p_k |D_k^{(n)}\rangle\langle D_k^{(n)}|$, the measured correlator becomes $C(t) = \mathrm{Tr}(\rho\, e^{-i\mathcal{H}t}) = \sum_k p_k e^{-iE_k t}$, so the interferometric signal directly represents a weighted spectral average over symmetric sectors. Thus, mixedness arising from imperfect preparation, dephasing, or intentional classical weighting is inherently incorporated in the measured autocorrelation, and no circuit modification is required.

Formally, the equivalence between this averaged Hadamard–test measurement and a true mixed–state expectation can be seen by expanding the coherent probe $|\psi\rangle = \frac{1}{\sqrt{N}}\sum_e |e\rangle$ on a computational basis. The interferometric estimator yields

$$\langle\psi|e^{-i\mathcal{H}t}|\psi\rangle = \frac{1}{N}\sum_{e,e'}\langle e'|e^{-i\mathcal{H}t}|e\rangle = \frac{1}{N}\sum_{e}\langle e|e^{-i\mathcal{H}t}|e\rangle + \frac{1}{N}\sum_{e\neq e'}\langle e'|e^{-i\mathcal{H}t}|e\rangle. \tag{S76}$$

The first term corresponds exactly to the mixed–state trace $\mathrm{Tr}(\rho\, e^{-i\mathcal{H}t})$ for $\rho = \frac{1}{N}\sum_e |e\rangle\langle e|$, whereas the second term contains off–diagonal coherences between distinct basis states. Under temporal averaging or random–phase dephasing, these cross terms vanish because their phases oscillate at frequencies $\omega_{e'} - \omega_e$, leading to

$$\overline{\langle\psi|e^{-i\mathcal{H}t}|\psi\rangle} = \frac{1}{N}\sum_{e}\langle e|e^{-i\mathcal{H}t}|e\rangle = \mathrm{Tr}(\rho\, e^{-i\mathcal{H}t}). \tag{S77}$$

Hence, the Hadamard test on a uniform superposition state reproduces the expectation value of an incoherent statistical ensemble without requiring any additional ancilla or explicit purification. In other words, quantum interference within the single Hadamard–test circuit naturally performs the same linear averaging that would otherwise arise from tracing out an ancillary subsystem in a purified mixed state.

A tapered discrete transform with window w_k (e.g., Hann) is then formed as

$$\tilde{C}(\omega_\ell) = \sum_{k=0}^{T-1} w_k\, C(t_k)\, e^{i\omega_\ell t_k}, \qquad \omega_\ell = \frac{2\pi\ell}{T\Delta t}, \;\; \ell = 0, \ldots, T-1, \tag{S78}$$

given frequency resolution $\Delta\omega = 2\pi/(T\Delta t)$ over the unaliased band $[0, \pi/\Delta t]$. With M repetitions per t_k, shot noise is approximately white with

$$\mathrm{SE}[C(t_k)] \simeq \sqrt{\frac{1 - |C(t_k)|^2}{M}}, \tag{S79}$$

and is shaped by the window response $|W(\omega)|$ in $|\tilde{C}(\omega)|$. Eigenfrequencies appear as peaks of $|\tilde{C}(\omega)|$; letting ω_ℓ be a discrete maximizer with neighbors $A_- = |\tilde{C}(\omega_{\ell-1})|$, $A_0 = |\tilde{C}(\omega_\ell)|$, $A_+ = |\tilde{C}(\omega_{\ell+1})|$, quadratic interpolation refines the location and amplitude,

$$\delta = \frac{1}{2}\,\frac{A_- - A_+}{A_- - 2A_0 + A_+}, \qquad \hat{\omega} = \omega_\ell + \delta\,\Delta\omega, \qquad \hat{A} = A_0 - \frac{(A_- - A_+)^2}{8\,(A_- - 2A_0 + A_+)}. \tag{S80}$$

For SUSY blocks probing H_1, a zero mode manifests near $\omega \approx 0$; to avoid leakage, a guard width $\Omega_{\mathrm{g}} = \kappa\,\Delta\omega$ with $\kappa \in [1, 3]$ is enforced and the smallest positive frequency is estimated as

$$\hat{\gamma} = \min\{\hat{\omega}_i :\; \hat{\omega}_i > \Omega_{\mathrm{g}}\}, \qquad \hat{\xi} = 1/\hat{\gamma}. \tag{S81}$$

If no zero mode is present, the two lowest refined peaks yield $\hat{E}_0$, $\hat{E}_1$, and the gap $\hat{\gamma} = \hat{E}_1 - \hat{E}_0$.

To cross-check FFT peaks, a parametric estimator fits a sum of complex exponentials to $\{C(t_k)\}$ via a shift-invariant method (Prony/ESPRIT): Hankel matrices (H_0, H_1) are formed, an effective rank $\hat{r}$ is chosen by SVD thresholding, and the generalized eigenproblem $H_1 v = \lambda H_0 v$ yields $z_j \approx e^{-iE_j\Delta t}$ and hence $\hat{E}_j = -\arg(z_j)/\Delta t$. Sweeping $\hat{r}$ over a small range and intersecting stable roots returns a smallest positive consistent element $\hat{\gamma}_{\mathrm{Prony}}$ that is compared against the windowed-DFT estimate.

Phase wrap-around is controlled by enforcing $\|\mathcal{H} - c_I I\| < \pi/\Delta t$ (via norm or Gershgorin bounds). Ambiguities are further disambiguated by acquiring a secondary dataset with spacing $\Delta t'$ whose ratio to Δt is far from low-order rationals; a true line must lie in the intersection

$$\mathcal{A}(\Delta t) = \left\{\hat{\omega}^{(\Delta t)} + \tfrac{2\pi m}{\Delta t}\right\}, \quad \mathcal{A}(\Delta t') = \left\{\hat{\omega}^{(\Delta t')} + \tfrac{2\pi m'}{\Delta t'}\right\}, \tag{S82}$$

from which the unique joint solution within the interpolation error bars is selected. A dedicated zero-mode test compares the near-zero band power to its sidebands (*94, 95*),

$$\mathcal{P}_0 = \sum_{|\omega_\ell| \le \Omega_z} |\tilde{C}(\omega_\ell)|^2, \qquad \mathcal{P}_{\mathrm{sb}} = \tfrac{1}{2} \sum_{\Omega_z < |\omega_\ell| \le 2\Omega_z} |\tilde{C}(\omega_\ell)|^2, \tag{S83}$$

and declares a zero mode when $R = \mathcal{P}_0/\mathcal{P}_{\mathrm{sb}}$ exceeds a calibrated threshold, stabilizing β_1 counting against spectral leakage.

The final aggregation combines the smallest nonzero from the refined FFT and Prony/ESPRIT via a conservative median,

$$\hat{\gamma} = \mathrm{median}\big(\hat{\gamma}_{\mathrm{FFT}},\ \hat{\gamma}_{\mathrm{Prony}}\big)\,, \tag{S84}$$

optionally weighted by inverse residuals (peak-fit error vs. reconstruction error). Uncertainty is quantified by a block bootstrap over time: resampling $\{C(t_k)\}$ in blocks at least as wide as the window main lobe yields $\{\hat{\gamma}^{(b)}\}$ for percentile intervals. Near an isolated line, a fast error proxy is

$$\mathrm{SE}[\hat{\omega}] \approx \frac{\beta_{\mathrm{win}}\,\Delta\omega}{\rho}, \quad \rho = \hat{A}/\sigma, \tag{S85}$$

with window constant β_{win} (Hann: ≈ 0.5) and peak SNR ρ; for zero mode, $\mathrm{SE}[\hat{\gamma}] = \mathrm{SE}[\hat{\omega}_1]$, otherwise, the two lowest-peak errors add in quadrature. A Cramér–Rao proxy,

$$\mathrm{Var}(\hat{E}) \ \gtrsim\ \frac{\sigma^2}{\sum_k a_{\mathrm{eff}}^2\, t_k^2}, \tag{S86}$$

emphasizes the value of a longer total span $T\Delta t$.

Resource–accuracy tradeoffs follow from the target gap $\gamma_\star$, requiring $T\Delta t \gtrsim 2\pi/\gamma_\star$. A decrease in Δt enlarges the Nyquist band but increases the number of controlled evolutions for a fixed span, with total sampling cost $T \times M$. Trotterized simulation of $e^{-i\mathcal{H}t}$ with step δt incurs

$$\|e^{-i\mathcal{H}t} - \tilde{U}(t)\| = O\big(t^2 \max_{\ell \ne \ell'} \|[H_\ell, H_{\ell'}]\|\big), \tag{S87}$$

while a symmetric second-order formula reduces this to $O(t^3)$. Short-term calibration points verify linear phase growth, and slow drifts are removed via a global linear fit prior to spectral estimation. The spectral entropy $S_{\mathrm{spec}} = -\sum_i p_i \log p_i$ computed from line strengths $p_i = \hat{A}_i / \sum_j \hat{A}_j$ summarizes mode complexity and is reported alongside $\hat{\gamma}$.

Peak identification from $|\tilde{C}(\omega)|$ follows a robust spectral-gap picking procedure. After applying a Hann window and detrending to suppress DC leakage, the analysis is restricted to a fixed search band $[w_{\mathrm{lo}}, w_{\mathrm{hi}}] = [0, 0.8]$ within the Nyquist interval. Within this band, candidate peaks are local maxima that exceed a robust threshold $T = \mathrm{median}(S) + 1.4826\, k_\sigma\, \mathrm{MAD}(S)$, which suppresses noise-dominated fluctuations. Each candidate is refined via parabolic interpolation for subbin accuracy, and optional harmonic guards exclude integer multiples of an estimated fundamental frequency ω_{est} within tolerance δ_{harm}. A selection policy then determines the representative spectral line: *nearest_to_estimate* chooses the candidate closest to ω_{est} (default), whereas *min_significant* or *lowest_nonzero* favour the smallest nonzero significant peak. If no valid candidate remains, the strongest in-band maximum serves as fallback. This combination of band restriction, DC/harmonic guards, and median–MAD thresholding yields a stable and noise-resilient estimate of the fundamental spectral gap.

An end-to-end procedure thus proceeds as follows: acquire complex correlators on a primary grid (and optionally a secondary $\Delta t'$), form windowed spectra, detect and refine peaks via (S80), apply zero-mode and alias guards, crosscheck with Prony/ESPRIT, aggregate to $\hat{\gamma}$ with a confidence interval, and finally report $\hat{\xi} = 1/\hat{\gamma}$ together with $\{p_i\}$ and S_{spec} and calibration diagnostics. For systems of ∼10–15 qubits, grouped Pauli–projector synthesis keeps each long-time controlled evolution at practical depth while preserving near-zero multiplicities and the first spectral gap with subpercent bias under noiseless calibration.

S12 Proof of the Spectral Bound between Energy Gap and Persistence

We derive a spectral bound that relates the Laplacian energy gap to the persistence of topological features observed during a filtration $\{K_t\}$. The main theorem states that the persistence $(d-b)$ of a homological feature born at $t=b$ and disappearing at $t=d$ satisfies

$$\tilde{L}(d-b) + (p+1)d_{p,\max} \geq \lambda_{\beta_{p+1}}(\Delta_p(K_b)), \tag{S88}$$

where $\tilde{L}$ denotes the effective Lipschitz constant of spectral variation, and where $d_{p,\max}$ is the maximal number of adjacent $(p-1)$–simplices for any p–simplex. A larger local spectral gap shortens the persistence, whereas a vanishing gap leads to long-lived harmonic modes.

First, recall that for any Hermitian matrix H, the Courant–Fischer theorem expresses the k-th eigenvalue as

$$\lambda_k(H) = \min_{\dim U=k} \max_{x\in U\setminus\{0\}} \frac{x^\mathsf{T} H x}{x^\mathsf{T} x} = \max_{\dim V=n-k+1} \min_{x\in V\setminus\{0\}} \frac{x^\mathsf{T} H x}{x^\mathsf{T} x}. \tag{S89}$$

If $H = U^\dagger \Lambda U$ with eigenvalues $\lambda_1 \leq \cdots \leq \lambda_n$ and $Ux = \alpha$, then

$$R_H(x) = \frac{\sum_i \lambda_i \alpha_i^2}{\sum_i \alpha_i^2} = \sum_i \lambda_i \tilde{\alpha}_i^2, \qquad \tilde{\alpha}_i = \frac{\alpha_i}{\|x\|}, \tag{S90}$$

so that $\max_{x\in\mathrm{span}\{e_1,\ldots,e_k\}} R_H(x) = \lambda_k$.

Now consider a block Hermitian matrix

$$M = \begin{pmatrix} A & B \\ B^\dagger & C \end{pmatrix}, \qquad S = A - BC^{-1}B^\dagger,$$

with A Hermitian and $C > 0$. At the minimizing point $y^*(x) = -C^{-1}B^\dagger x$, the Rayleigh quotient satisfies

$$R_M(x, y^*(x)) = R_S(x)\Big(1 + \frac{\|y^*(x)\|^2}{\|x\|^2}\Big)^{-1} \leq R_S(x), \tag{S91}$$

and from the min–max relation one obtains

$$\lambda_k(M) \leq \lambda_k(S), \qquad \lambda_{k+d}(M) \geq \lambda_k(S), \tag{S92}$$

where $d = \dim(C)$. Applying this result to $\Delta_p(K_t)$ and its persistent form $\Delta_p^{(s,t)}$ yields

$$\lambda_k(\Delta_p(K_t)) \leq \lambda_k(\Delta_p^{(s,t)}) \leq \lambda_{k+d}(\Delta_p(K_t)). \tag{S93}$$

Next, note that the p–Laplacian algorithm decomposes into upwards and downwards components:

$$\Delta_p = \Delta_{p,\mathrm{up}} + \Delta_{p,\mathrm{down}}, \qquad \Delta_{p,\mathrm{up}} = \partial_{p+1}\partial_{p+1}^{\dagger},\ \Delta_{p,\mathrm{down}} = \partial_p^{\dagger}\partial_p.$$

The upwards part represents $(p+1)$–dimensional fillings, whereas the downwards part encodes adjacency among $(p-1)$–simplices. The Schur relation applied to $\Delta_{p,\mathrm{up}}$ yields

$$\lambda_k(\Delta_{p,\mathrm{up}}(K_t)) \le \lambda_k(\Delta_{p,\mathrm{up}}^{(s,t)}) \le \lambda_{k+d}(\Delta_{p,\mathrm{up}}(K_t)). \tag{S94}$$

Because $\Delta_p = \Delta_{p,\mathrm{up}} + \Delta_{p,\mathrm{down}}$, the following bounds hold:

$$\lambda_k(\Delta_p(K_t)) \ge \lambda_k(\Delta_{p,\mathrm{up}}(K_t)) + \lambda_{\min}(\Delta_{p,\mathrm{down}}(K_t)), \tag{S95}$$

$$\lambda_k(\Delta_p(K_t)) \le \lambda_k(\Delta_{p,\mathrm{up}}(K_t)) + \lambda_{\max}(\Delta_{p,\mathrm{down}}(K_t)). \tag{S96}$$

Combining these gives a two-sided interlacing for the persistent Laplacian:

$$\begin{aligned}\lambda_k(\Delta_p(K_t)) - \lambda_{\max}\big(\Delta_{p,\mathrm{down}}(K_t)\big) + \lambda_{\min}\big(\Delta_{p,\mathrm{down}}(K_s)\big)& \\ \le\ \lambda_k\big(\Delta_p^{(s,t)}\big)\ \le\ \lambda_{k+d}\big(\Delta_p(K_t)\big) - \lambda_{\max}\big(\Delta_{p,\mathrm{down}}(K_s)\big) + \lambda_{\min}\big(\Delta_{p,\mathrm{down}}(K_t)\big).&\end{aligned} \tag{S97}$$

This shows that the spectrum of the persistent Laplacian is bounded between those of the ordinary Laplacian, with corrections governed by the spectral range of $\Delta_{p,\mathrm{down}}$.

To relate these bounds to geometric variation, consider the inequality between two Hermitian matrices A and B:

$$x^{\mathsf{T}}Bx = x^{\mathsf{T}}Ax + x^{\mathsf{T}}(B-A)x \le x^{\mathsf{T}}Ax + \|B-A\|\|x\|^2. \tag{S98}$$

Taking the infimum over all normalized x yields

$$\lambda_k(B) \le \lambda_k(A) + \|B-A\|. \tag{S99}$$

If the Laplacian varies Lipschitz-continuously with respect to t,

$$\|\Delta_p(K_t) - \Delta_p(K_s)\| \le L|t-s|, \tag{S100}$$

then the corresponding eigenvalues satisfy

$$\lambda_k(\Delta_p(K_t)) \geq \lambda_k(\Delta_p(K_s)) - L|t-s|. \tag{S101}$$

The downwards Laplacian's spectral width provides a combinatorial correction term. Since

$$\text{width}(\Delta_{p,\text{down}}(K_s)) = \lambda_{\max} - \lambda_{\min} \leq (p+1)d_{p,\max}, \tag{S102}$$

where d_p denotes the maximum number of p-dimensional simplices that are adjacent to any given $(p-1)$-dimensional simplex σ, we obtain

$$\lambda_{\max}(\Delta_{p,\text{down}}(K_t)) - \lambda_{\min}(\Delta_{p,\text{down}}(K_s)) \leq (p+1)d_{p,\max} + L'(t-s), \tag{S103}$$

and thus the persistent Laplacian obeys

$$\lambda_k(\Delta_p^{(s,t)}) \geq \lambda_k(\Delta_p(K_s)) - \tilde{L}(t-s) - (p+1)d_{p,\max}, \qquad \tilde{L} = L + L'. \tag{S104}$$

The behavior of individual eigenmodes can be analysed perturbatively. For $H(\epsilon) = H_0 + \epsilon V$ with $\epsilon \ll 1$,

$$E_m = E_m^{(0)} + \epsilon\langle\phi_m, V\phi_m\rangle + \epsilon^2 \sum_{n\neq m} \frac{|\langle\phi_m, V\phi_n\rangle|^2}{E_m^{(0)} - E_n^{(0)}} + \cdots. \tag{S105}$$

If $E_0^{(0)} = 0$ is isolated, it remains zero until the degeneracy is lifted, as shown in Kato's *Perturbation Theory for Linear Operators* (*96*). Hence, a homological feature persists while its Laplacian mode stays within the zero eigenspace:

$$\lambda_{\beta_{p+1}}(\Delta_p^{(b,t)}) \approx 0 \ (t < d), \qquad \lambda_{\beta_{p+1}}(\Delta_p^{(b,d)}) > 0. \tag{S106}$$

The stability of the zero eigenspace can be formalized via the Riesz projector

$$\Pi_0(t) = \frac{1}{2\pi i} \oint_{\Gamma_t} (zI - \Delta_p(K_t))^{-1}\, dz, \tag{S107}$$

where Γ_t encloses the isolated eigenvalue 0. If $E = \Delta_p(K_t) - \Delta_p(K_s)$, then

$$\|\Pi_0(t) - \Pi_0(s)\| \leq \frac{\|E\|}{\gamma_s} \leq \frac{L}{\gamma_s}|t-s|. \tag{S108}$$

As long as $L|t - s| < \gamma_s = \lambda_1(\Delta_p(K_s))$, the rank of the projector—and therefore the Betti number—remains invariant:

$$\operatorname{rank} \Pi_0(t) = \operatorname{rank} \Pi_0(s). \tag{S109}$$

A death of homology thus requires that the spectral gap γ closes.

When a homological feature is born at $t = b$, the smallest nonzero eigenvalue $\lambda_{\beta_{p+1}}(\Delta_p(K_b))$ defines a local energy gap. As filtration continues, this feature persists as long as $\lambda_{\beta_{p+1}}(\Delta_p^{(b,t)}) \simeq 0$. Its eventual disappearance at $t = d$ occurs when this zero mode lifts to a finite value. When the spectral inequality (S104) is used, this transition can only occur if

$$\lambda_{\beta_{p+1}}(\Delta_p(K_b)) - \tilde{L}(d - b) - (p + 1)d_{p,\max} \leq 0, \tag{S110}$$

which rearranges to the quantitative persistence condition

$$\tilde{L}(d - b) + (p + 1)d_{p,\max} \geq \lambda_{\beta_{p+1}}(\Delta_p(K_b)). \tag{S111}$$

In other words, the death of a homological feature requires that the cumulative spectral variation across (b, d) surpasses the initial Laplacian energy gap at b. If this threshold is not reached, the zero mode—and hence the topological feature—remains stable.

Finally, because the Laplacian encodes gradients, curls, and divergences of the field, its eigenvalues describe the curvature of the local energy landscape. A large spectral gap λ_1 corresponds to strong restoring forces that stabilize the topology, whereas $\lambda_1 \to 0$ represents a topological phase transition where harmonic modes emerge. The ordinary Laplacian gap thus quantifies the robustness of homological structures: the closure of this gap signals the annihilation of a topological cycle. Equation (S111) unifies energy-gap dynamics and persistent homology by showing that the local spectral curvature (or SUSY energy gap) provides a quantitative bound on the persistence of homological features, offering a spectral–geometric interpretation of topological stability consistent with the SUSY behavior observed in the Lorenz system.

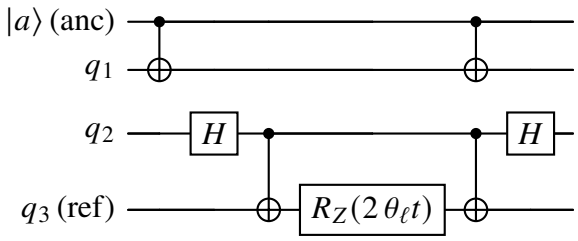

Figure S1: Controlled time evolution for one local term $U_\ell(t) = e^{-i\,\theta_\ell t\,P_{q_1}\otimes P_{q_2}\otimes P_{q_3}}$. Basis rotations convert X/Y to Z, CNOTs collect parity on q_3, and an ancilla-controlled $R_Z(2\theta_\ell t)$ realizes the exponential.

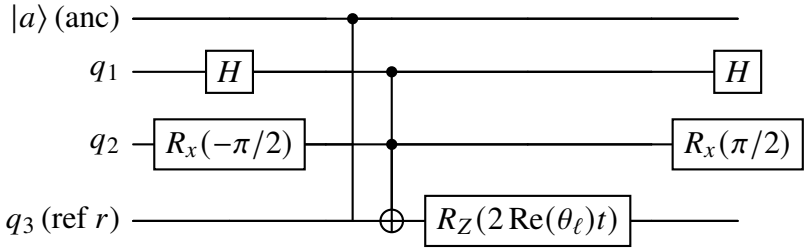

Figure S2: Controlled time evolution for one local factor $U_\ell(t) = e^{-i\,\theta_\ell t\,\bigotimes_{q\in S_\ell} P_q^{(\ell)}}$. Here $P_{q_1} = X$, $P_{q_2} = Y$, $P_{q_3} = Z$. CNOTs collect the Z-parity onto the rightmost reference qubit $r = q_3$; an ancilla-controlled $R_Z(2\,\mathrm{Re}(\theta_\ell)t)$ implements the phase; then,they uncompute.

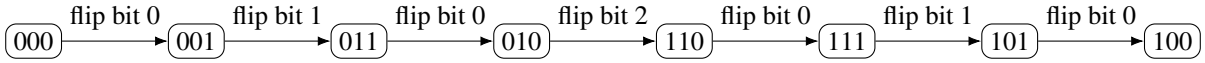

Figure S3: Gray-order traversal of a 3-bit control mask. Consecutive masks differ by a single bit, minimizing the number of control toggles (X gates) between terms that share the same Pauli-letter pattern.

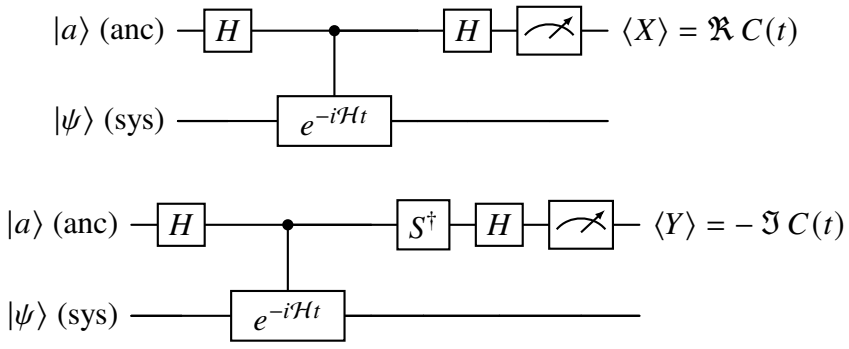

Figure S4: Hadamard-test circuits for a single sample time t. The controlled-$e^{-i\mathcal{H}t}$ block is synthesized as $U_{\mathrm{ctrl}}(t)$ (Sec. S10). Measuring X (top) yields $\Re\, C(t)$; inserting $S^\dagger$ and then measuring X (bottom) yields $-\,\Im\, C(t)$.

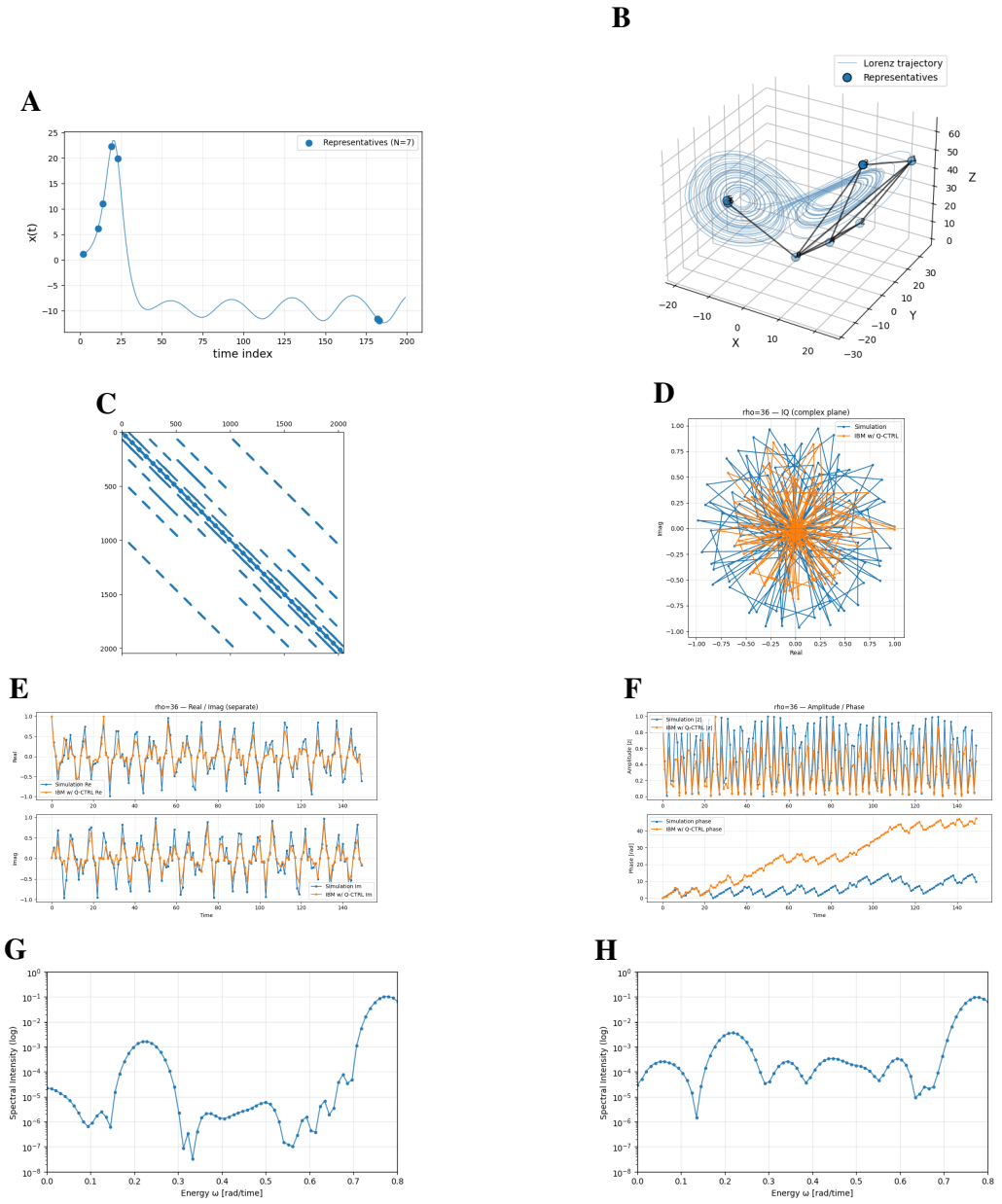

$\rho = 36$

Figure S5: **Quantum and classical diagnostics for the Lorenz system at** $\rho = 36$**.** (**A**) Time-series input and (**B**) 3D attractor embedding. (**C**) Hodge Laplacian matrix and (**D**) complex-plane trajectory of the QPE amplitude. (**E**) Real-imaginary waveform, (**F**) amplitude-phase trace, and (**G**, **H**) QPE spectra from the simulation and IBM hardware. Broad, merged spectral peaks indicate weak topological separation in the early chaotic regime.

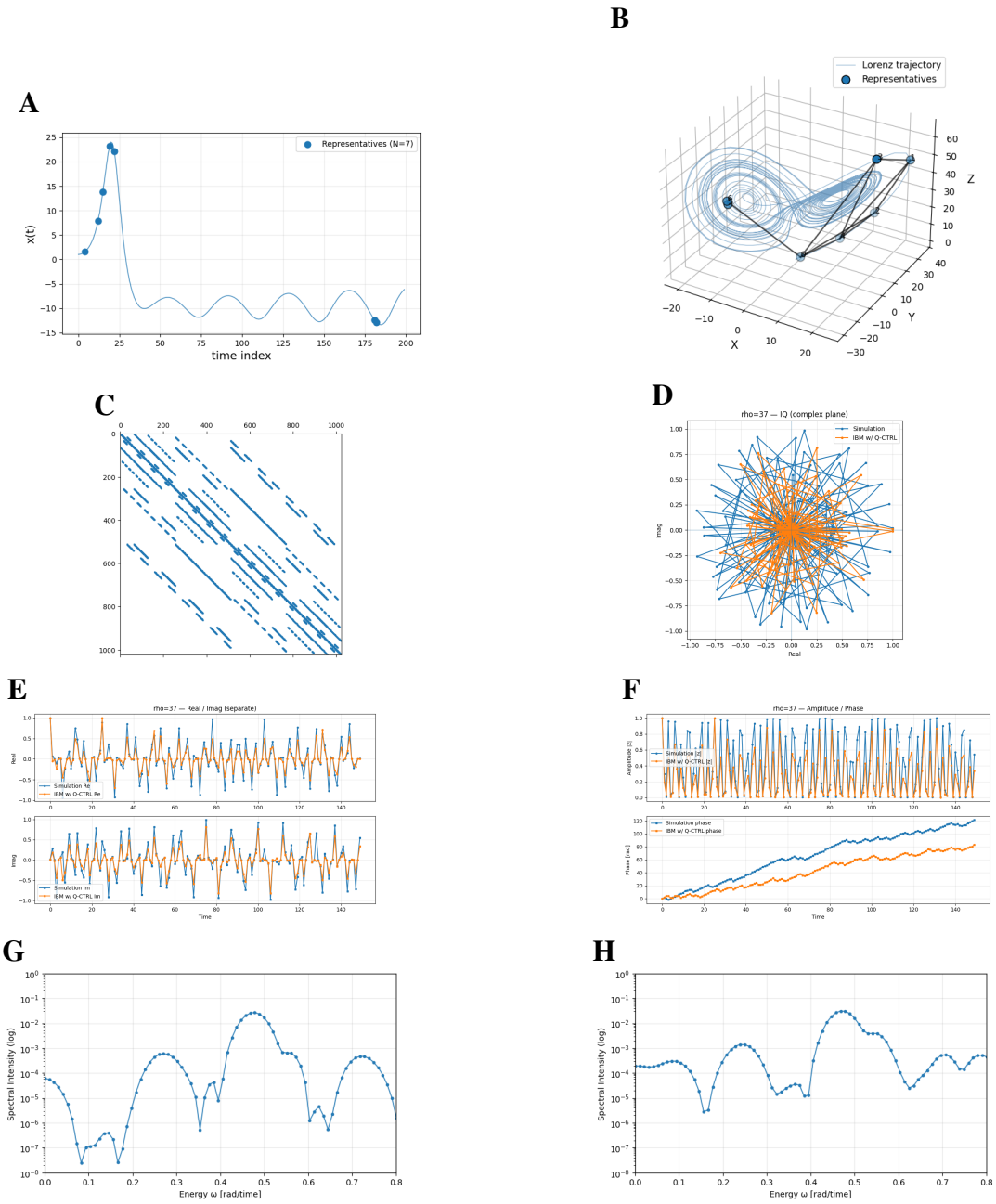

$\rho = 37$

Figure S5: **Quantum and classical diagnostics for the Lorenz system at** $\rho = 37$**.** Slight narrowing of spectral lines and partial clustering of low-frequency modes mark the initial development of the quasi-periodic structure.

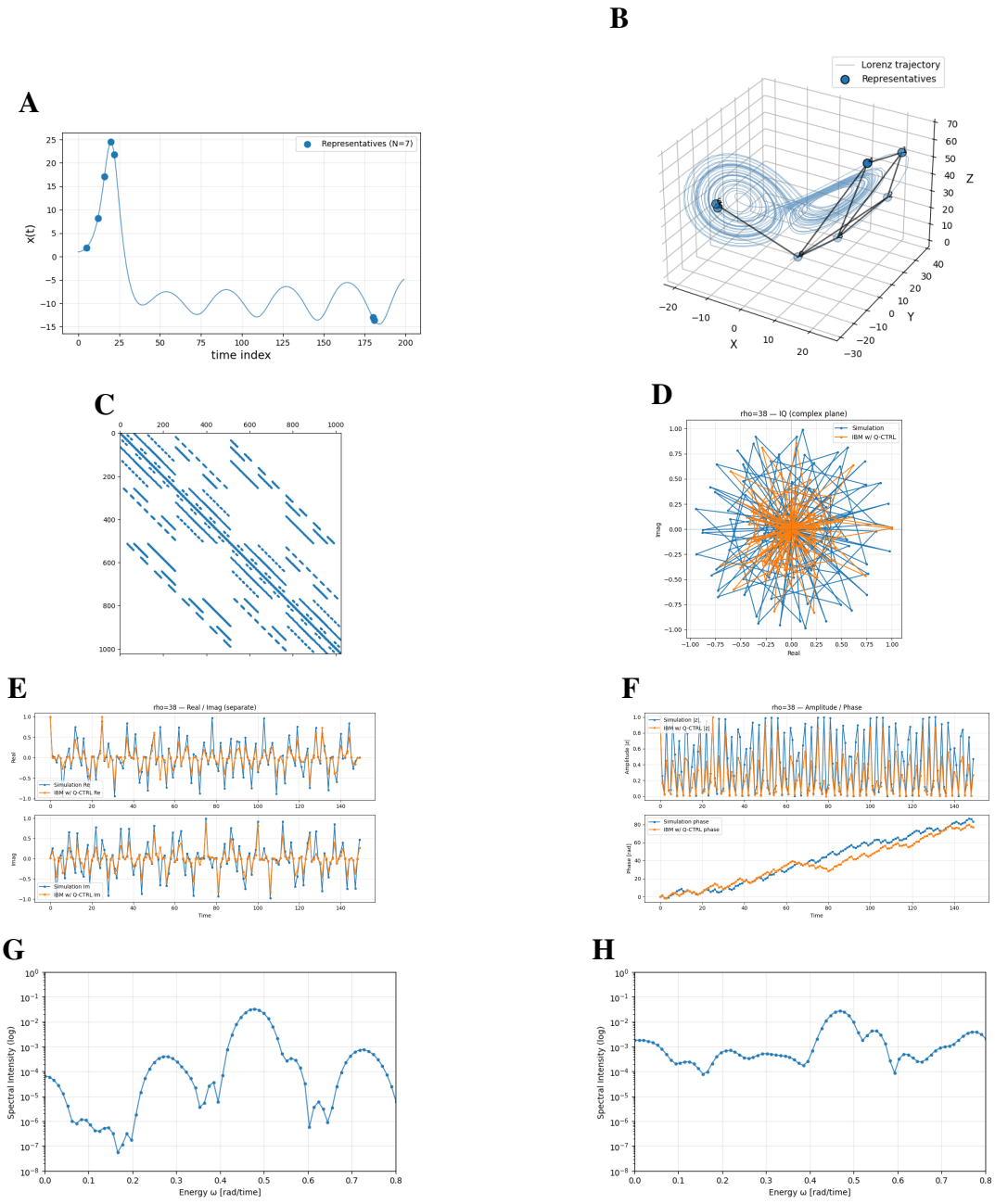

$\rho = 38$

Figure S5: **Quantum and classical diagnostics for the Lorenz system at $\rho = 38$.** Spectral entropy begins to decline, and distinct peaks emerge in both the simulator and hardware spectra, indicating partial organization of the attractor's loop geometry.

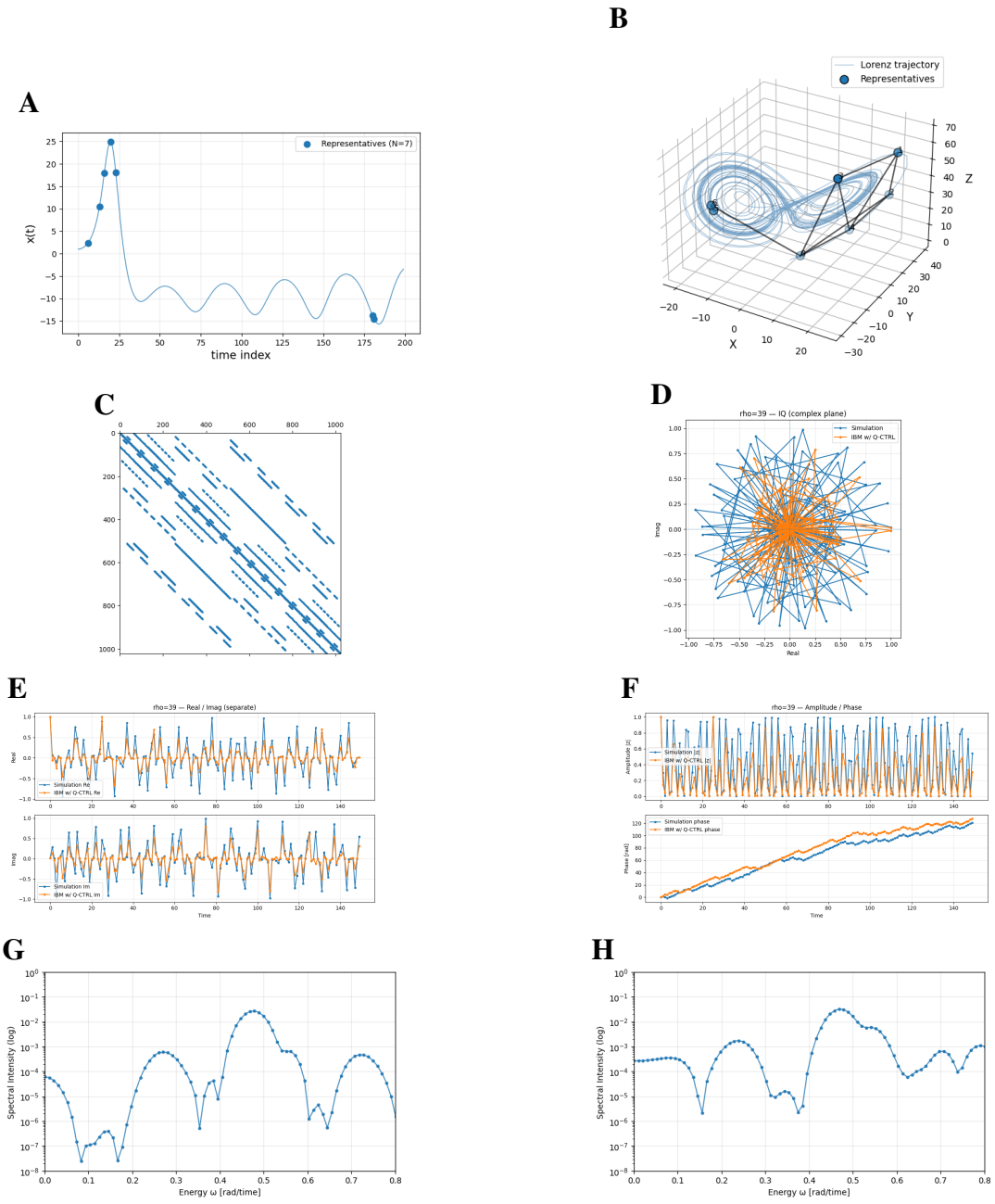

$\rho = 39$

Figure S5: **Quantum and classical diagnostics for the Lorenz system at $\rho = 39$.** Discrete peaks become more pronounced and near-zero components start to separate from the continuum. Topological coherence strengthens as the attractor approaches double-wing formation.

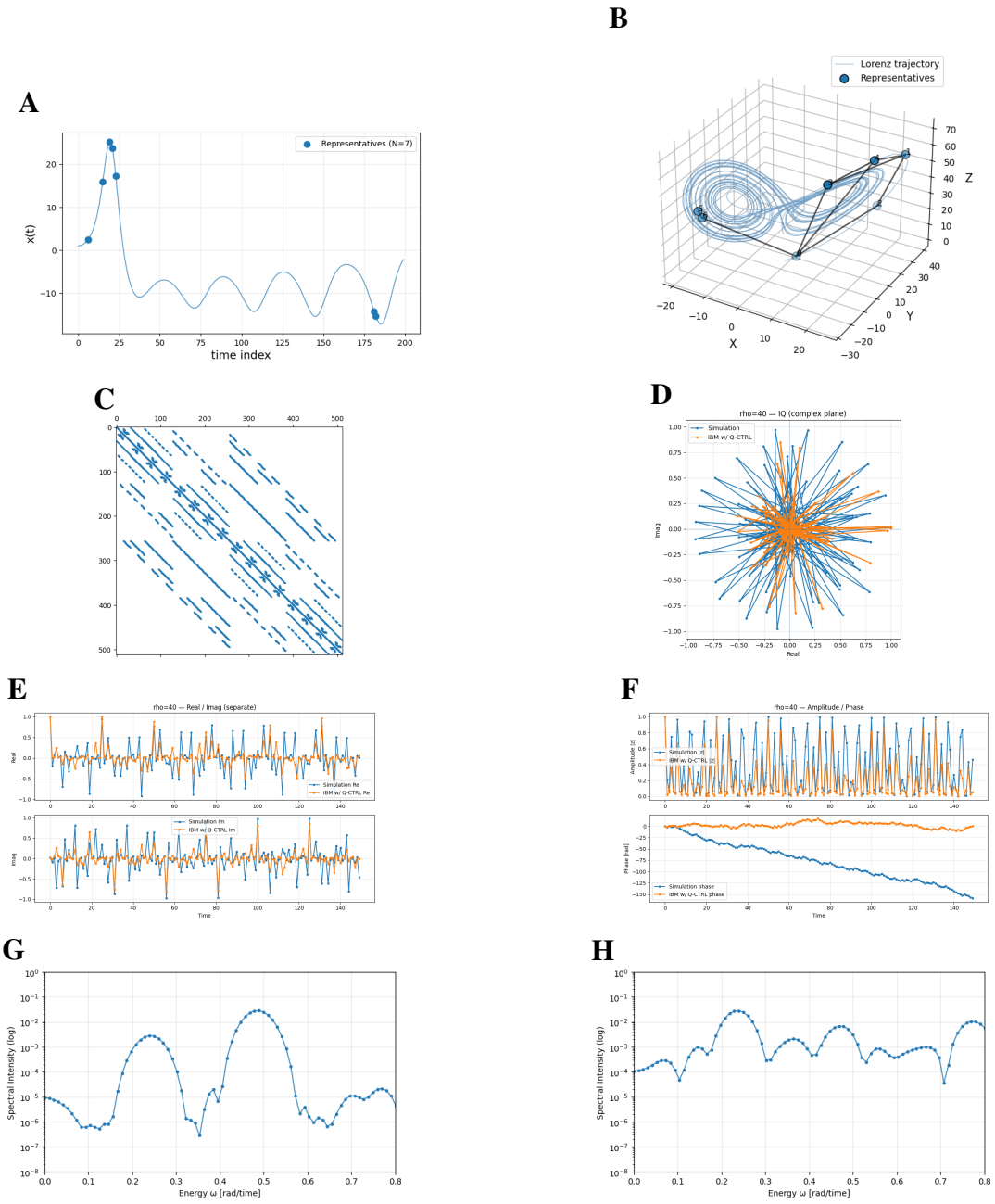

$\rho = 40$

Figure S5: **Quantum and classical diagnostics for the Lorenz system at** $\rho = 40$**.** Both the simulation and hardware show clear harmonic-mode isolation and maximal phase-space regularity. Near-zero clusters narrow sharply, marking the onset of topological stabilization.

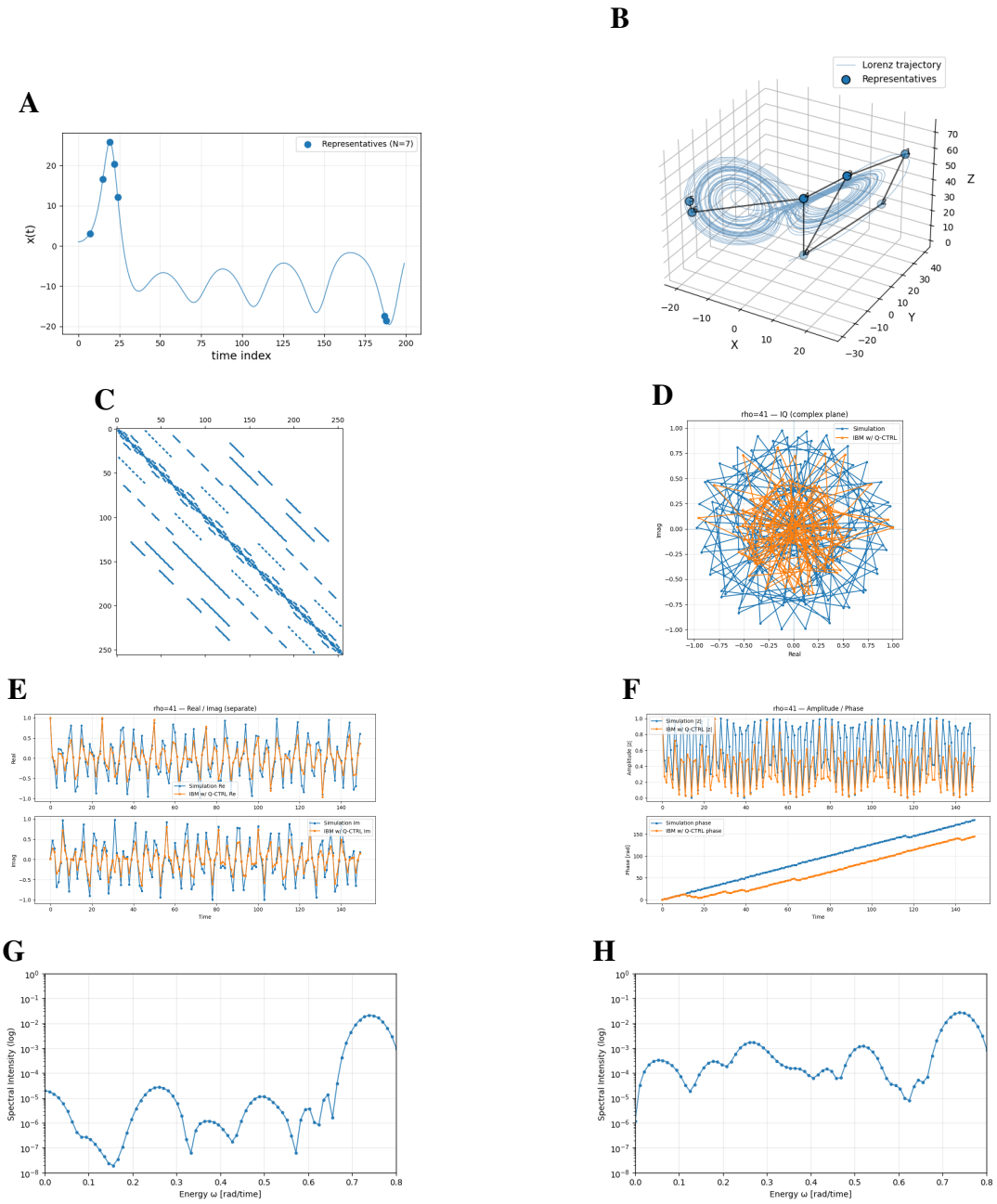

$\rho = 41$

Figure S5: **Quantum and classical diagnostics for the Lorenz system at $\rho = 41$.** The Hodge–Laplacian spectrum exhibits its widest gap and cleanest harmonic–excited separation, coinciding with maximal H_1 persistence. The complex-plane trajectories are nearly circular, confirming spectral coherence.

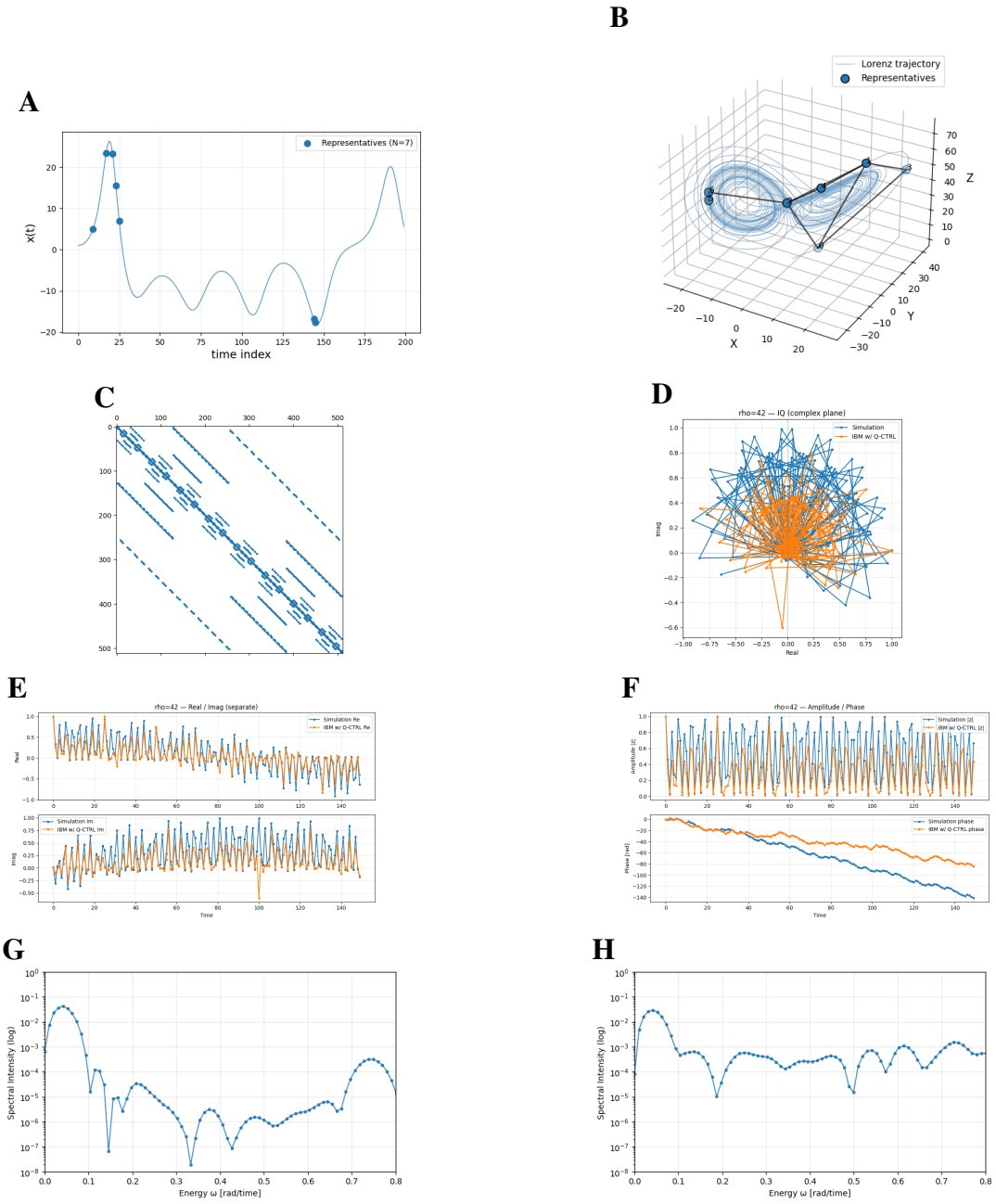

$\rho = 42$

Figure S5: **Quantum and classical diagnostics for the Lorenz system at** $\rho = 42$**.** Spectral broadening and partial peak overlap indicate the onset of *topological coherence breaking*, where harmonic modes lose phase alignment across scales. The harmonic sector remains visible but less isolated, marking the gradual destabilization of the coherent loop.

Table S1: **Summary of hardware specifications for `ibm_kingston`.** Error metrics refer to per-gate Pauli error rates at the calibration time; CLOPS denotes circuit layer operations per second.

Qubits	156
Processor type	Heron r2
QPU version	1.0.0
Basis gates	`cz, id, rx, rz, rzz, sx, x`
Best two-qubit error	8.88×10^{-4}
Two-qubit error (layered)	3.42×10^{-3}
Median CZ error	1.93×10^{-3}
Median SX error	2.372×10^{-4}
Median readout error	8.606×10^{-3}
Median T_1	$262.42\,\mu$s
Median T_2	$119.55\,\mu$s
CLOPS (throughput)	250 K